#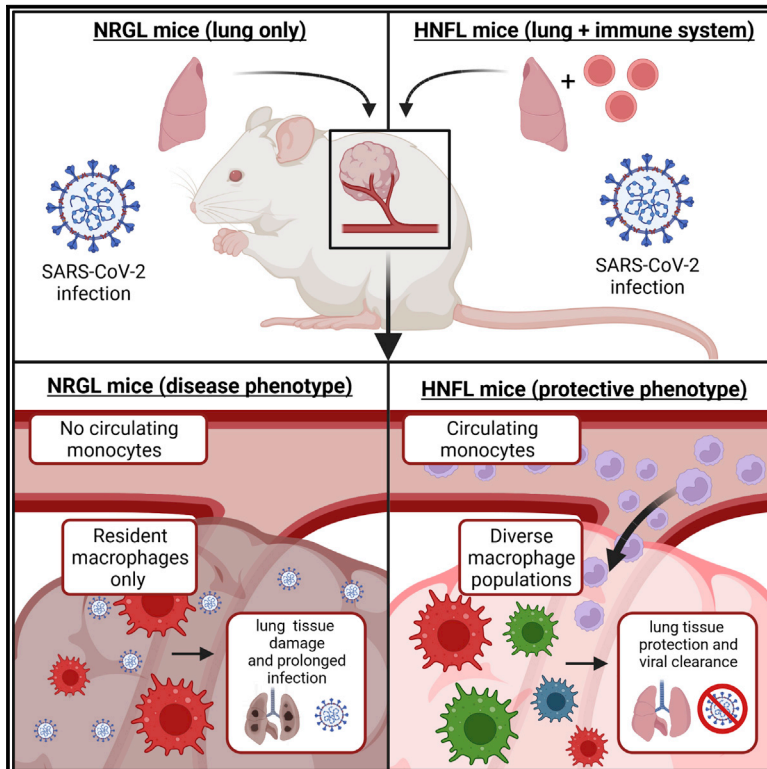 Humanized mice reveal a macrophage-enriched gene signature defining human lung tissue protection during SARS-CoV-2 infection

## Graphical abstract

## Authors

Devin J. Kenney, Aoife K. O'Connell, Jacquelyn Turcinovic, ..., Nicholas A. Crossland, Alexander Ploss, Florian Douam

## Correspondence

ncrossla@bu.edu (N.A.C.), aploss@princeton.edu (A.P.), fdouam@bu.edu (F.D.)

## In brief

Kenney et al. develop a mouse model co-engrafted with human lung xenografts (fLX) and a myeloid-enriched immune system (HNFL mice). While mice solely engrafted with fLX are highly susceptible to SARS-CoV-2 infection, HNFL mice are protected from viral infection. Protection associates with upregulation of a specific macrophage-enriched gene signature.

## Highlights

- HNFL mice harbor human lung xenografts (fLX) and a myeloid-enriched immune system

- Mice solely engrafted with fLX are highly susceptible to SARS-CoV-2 infection

- HNFL mice are protected from SARS-CoV-2 infection and severe histopathology

- The upregulation of a macrophage-enriched signature of 11 genes defines protection

CellPress

## Resource

# Humanized mice reveal a macrophage-enriched gene signature defining human lung tissue protection during SARS-CoV-2 infection

Devin J. Kenney,[1,2,21] Aoife K. O'Connell,[1,2,21] Jacquelyn Turcinovic,[2,3,21] Paige Montanaro,[2,4,21] Ryan M. Hekman,[5,6,21] Tomokazu Tamura,[7,21] Andrew R. Berneshawi,[7] Thomas R. Cafiero,[7] Salam Al Abdullatif,[8,9] Benjamin Blum,[5,6] Stanley I. Goldstein,[5,6] Brigitte L. Heller,[7] Hans P. Gertje,[2,4] Esther Bullitt,[10] Alexander J. Trachtenberg,[1,2] Elizabeth Chavez,[1,2] Evans Tuekam Nono,[1,2] Catherine Morrison,[1,2] Anna E. Tseng,[1,2] Amira Sheikh,[1,2] Susanna Kurnick,[2,11,20] Kyle Grosz,[2,11] Markus Bosmann,[9,12] Maria Ericsson,[13] Bertrand R. Huber,[14] Mohsan Saeed,[2,6] Alejandro B. Balazs,[15] Kevin P. Francis,[16] Alexander Klose,[17] Neal Paragas,[17,18] Joshua D. Campbell,[8,9] John H. Connor,[1,2,21] Andrew Emili,[5,6,19,21] Nicholas A. Crossland,[2,4,21,*] Alexander Ploss,[7,21,*] and Florian Douam[1,2,21,22,*]

[1]Department of Microbiology, Boston University School of Medicine, Boston, MA, USA
[2]National Emerging Infectious Diseases Laboratories, Boston University, Boston, MA, USA
[3]Bioinformatics Program, Boston University, Boston, MA, USA
[4]Department of Pathology and Laboratory Medicine, Boston University School of Medicine, Boston, MA, USA
[5]Center for Network Systems Biology, Boston University, Boston, MA, USA
[6]Department of Biochemistry, Boston University School of Medicine, Boston, MA, USA
[7]Department of Molecular Biology, Princeton University, Princeton, NJ, USA
[8]Single Cell RNA Sequencing Core, Boston University, Boston, MA, USA
[9]Department of Medicine, Boston University School of Medicine, Boston, MA, USA
[10]Department of Physiology and Biophysics, Boston University School of Medicine, Boston, MA, USA
[11]Animal Science Center, Boston University, Boston, MA, USA
[12]Center for Thrombosis and Hemostasis, University Medical Center of the Johannes Gutenberg-University, Mainz 55131, Germany
[13]Electron Microscopy Core Facility, Harvard Medical School, Boston, MA, USA
[14]Department of Neurology, Boston University School of Medicine, Boston, MA, USA
[15]Ragon Institute of MGH, MIT and Harvard, Cambridge, MA, USA
[16]PerkinElmer, Hopkinton, MA, USA
[17]In Vivo Analytics, Inc., New York, NY, USA
[18]Department of Radiology Imaging Research Lab, University of Washington, Seattle, WA, USA
[19]Department of Biology, Boston University School of Medicine, Boston, MA, USA
[20]Present address: Center for Animal Resources and Education, Brown University, Providence, RI, USA
[21]These authors contributed equally
[22]Lead contact
*Correspondence: ncrossla@bu.edu (N.A.C.), aploss@princeton.edu (A.P.), fdouam@bu.edu (F.D.)
https://doi.org/10.1016/j.celrep.2022.110714

## SUMMARY

The human immunological mechanisms defining the clinical outcome of SARS-CoV-2 infection remain elusive. This knowledge gap is mostly driven by the lack of appropriate experimental platforms recapitulating human immune responses in a controlled human lung environment. Here, we report a mouse model (i.e., HNFL mice) co-engrafted with human fetal lung xenografts (fLX) and a myeloid-enhanced human immune system to identify cellular and molecular correlates of lung protection during SARS-CoV-2 infection. Unlike mice solely engrafted with human fLX, HNFL mice are protected against infection, severe inflammation, and histopathological phenotypes. Lung tissue protection from infection and severe histopathology associates with macrophage infiltration and differentiation and the upregulation of a macrophage-enriched signature composed of 11 specific genes mainly associated with the type I interferon signaling pathway. Our work highlights the HNFL model as a transformative platform to investigate, in controlled experimental settings, human myeloid immune mechanisms governing lung tissue protection during SARS-CoV-2 infection.

## INTRODUCTION

The immunological mechanisms driving susceptibility to coronavirus disease 2019 (COVID-19), a recent viral respiratory disease caused by severe acute respiratory syndrome coronavirus 2 (SARS-CoV-2) (Zhu et al., 2020), remain elusive. While human patient studies have been instrumental in uncovering immune correlates of severe disease (Bastard et al., 2020; Combes et al., 2021; Delorey et al., 2021; Hadjadj et al., 2020; Rendeiro et al., 2021; Wauters et al., 2021; Ziegler et al., 2021), these

studies are fraught with considerable limitations. While studies focusing on patients with mild/moderate infections are limited to immunological sampling of the peripheral blood, bronchioalveolar fluid (BALF), and nasopharynx, postmortem studies provide only a snapshot of diseased lung tissues. Interpretation of human studies is also compounded by several factors, including non-synchronized collection of tissues post-infection, interindividual variability, and co-morbidities.

Animal models provide increased control of experimental settings, allowing us to go beyond the descriptive nature of human studies. Non-human primates (NHPs), hamsters, and ferrets are naturally susceptible to SARS-CoV-2 infection and have been instrumental in evaluating the therapeutic potential and prophylactic efficacy of many antiviral countermeasures against this virus (Kim et al., 2020; Sia et al., 2020; Singh et al., 2021; Tostanoski et al., 2020; Vogel et al., 2021). However, in-depth understanding of SARS-CoV-2 pathogenesis and immunity in these models has been hindered by several limitations, including the limited reagent availability and restrictive costs associated with NHP studies and the large evolutionary divergence between humans and hamsters or ferrets, which manifests in vastly different immune responses and lung environments. In contrast to hamsters or ferrets, mice are poorly susceptible to several human coronaviruses, including SARS-CoV and most SARS-CoV-2 variants. While mice can be rendered permissive by transgenic approaches (McCray et al., 2007; Winkler et al., 2020) or via viral adaptation, the evolutionary divergence between mouse and human, reflected by significant differences in their immune system (Mestas and Hughes, 2004), also represents a major limitation for the use of this species in understanding human immune responses to viral infection.

Mice harboring human tissue xenografts have been used to investigate a variety of infectious diseases over the past three decades (Douam and Ploss, 2018). Recently, mice engrafted with human fetal lung xenografts (fLX) were successfully infected with several viruses, including coronaviruses (Wahl et al., 2019, 2021). Importantly, fLX were also engrafted into mice co-engrafted with human fetal liver, thymus, and hematopoietic stem cells (HSCs) (BLT mice, then yielding BLT-Lung/L mice), enabling the study of lymphoid responses to a wide range of viruses, including respiratory viruses. However, while the BLT platform remains a powerful system to explore cellular and humoral responses to viral infection (Dudek et al., 2012; Frias-Staheli et al., 2014; Wang et al., 2014), the myeloid compartment remains limited, preventing this model from recapitulating important early immunological events at the front line of a viral infection. The differential myeloid responses reported between patients with mild/moderate and severe COVID-19 (Rendeiro et al., 2021; Wauters et al., 2021) are a prominent demonstration of the importance of modeling myeloid responses to accurately capture molecular mechanisms defining the clinical outcome of an infection.

In this study, we aimed to develop and characterize a humanized mouse model recapitulating protective human myeloid responses to SARS-CoV-2 within a human lung environment. We previously reported that immunodeficient NOD-$Rag1^{-/-}IL2R\gamma^{NULL}$ (NRG) mice defective for fetal liver kinase 2 expression (NRG-Flk2$^{-/-}$ or NRGF) display a selective expansion of the human myeloid and

natural killer (NK) cell compartments over conventional humanized mouse models upon expression of human FMS-related receptor tyrosine kinase 3 ligand (hFlt3LG), the ligand of Flk2 (Douam et al., 2018). Here, we co-engrafted NRGF mice with a pair of fLX prior to injection of allogeneic human HSCs and adeno-associated virus expressing hFlt3LG (AAV-Flt3LG), yielding HIS-NRGF/Flt3LG-L (referred to as HNFL) mice. While SARS-CoV-2 inoculation of fLX engrafted into immunodeficient NRG or NRGF mice (NRG/F-L) resulted in persistent infection and severe histopathology, HNFL mice were effectively protected against SARS-CoV-2 infection without exhibiting any signs of severe tissue damage. Protection in HNFL mice was associated with significant macrophage infiltration and differentiation and was defined by the upregulation of a macrophage-enriched signature composed of 11 specific genes/proteins (protection-defining genes), which included USP18, a negative regulator of type I interferon (IFN) responses and ISGylation (Basters et al., 2018).

Altogether, we demonstrate that HNFL mice represent a powerful, amenable, and cost-effective platform to uncover myeloid-mediated mechanisms defining the clinical and histopathological outcomes of SARS-CoV-2 infection in a human lung environment.

## RESULTS

### Generation of the HNFL model

Ten- to fifteen-week-old male and female NRG mice were surgically implanted subcutaneously with two pieces of fetal lung tissue, one on each side of the animal's thoracic body wall (Figure 1A). Following engraftment, all animals were healthy and displayed macroscopically detectable fLX on both sides of their body (Figures 1A and S1A). Macroscopic and histological analysis illustrated interstitial infiltration of fLX by murine blood vessels with retention of human vasculature (Figures S1B–S1D). Cells appeared histologically normal without any evidence of degeneration and/or necrosis (Figures S1E–S1N). Different stages of fetal lung maturation were associated with differential expression of ACE2, pro-surfactant protein C (SFTPC) (an alveolar type 2 [AT2] pneumocyte differentiation marker), and human-specific CD31 (blood vessel marker) (Figures S1E–S1N).

For HNFL mouse generation, 10- to 15-week-old NRGF mice were engrafted with pairs of fLX 3 to 5 weeks prior to injection of allogeneic human HSCs (Figure 1B) and AAV-hFlt3LG. From here on, fLX of NRGL and HNFL mice will be referred to as NRGL-LX or HNFL-LX, respectively. Flow cytometric analysis showed a significant increase in the frequency of human CD45$^+$cells in HNFL-LX compared with NRGL-LX (Figures 1C and S2A). Single-cell RNA sequencing (scRNA-seq) confirmed an increased frequency of human cells in HNFL-LX (84.25% versus 67.14% in NRGL) (Figures 1D–1G; Table S1), which was predominantly hematopoietically mediated (48.41% human hematopoietic cells versus 51.59% non-hematopoietic; 13.26% versus 86.74% in NRGL) (Figures 1E and 1G). The lung epithelial compartment looked similar in composition between NRGL-LX and HNFL-LX, with an AT2 subcompartment encompassing 47.7% of total epithelial subsets versus 50.2%, respectively (Figure S2B). Consistently, differential human ACE2 expression was not observed between NRGL-LX and HNFL-LX mice
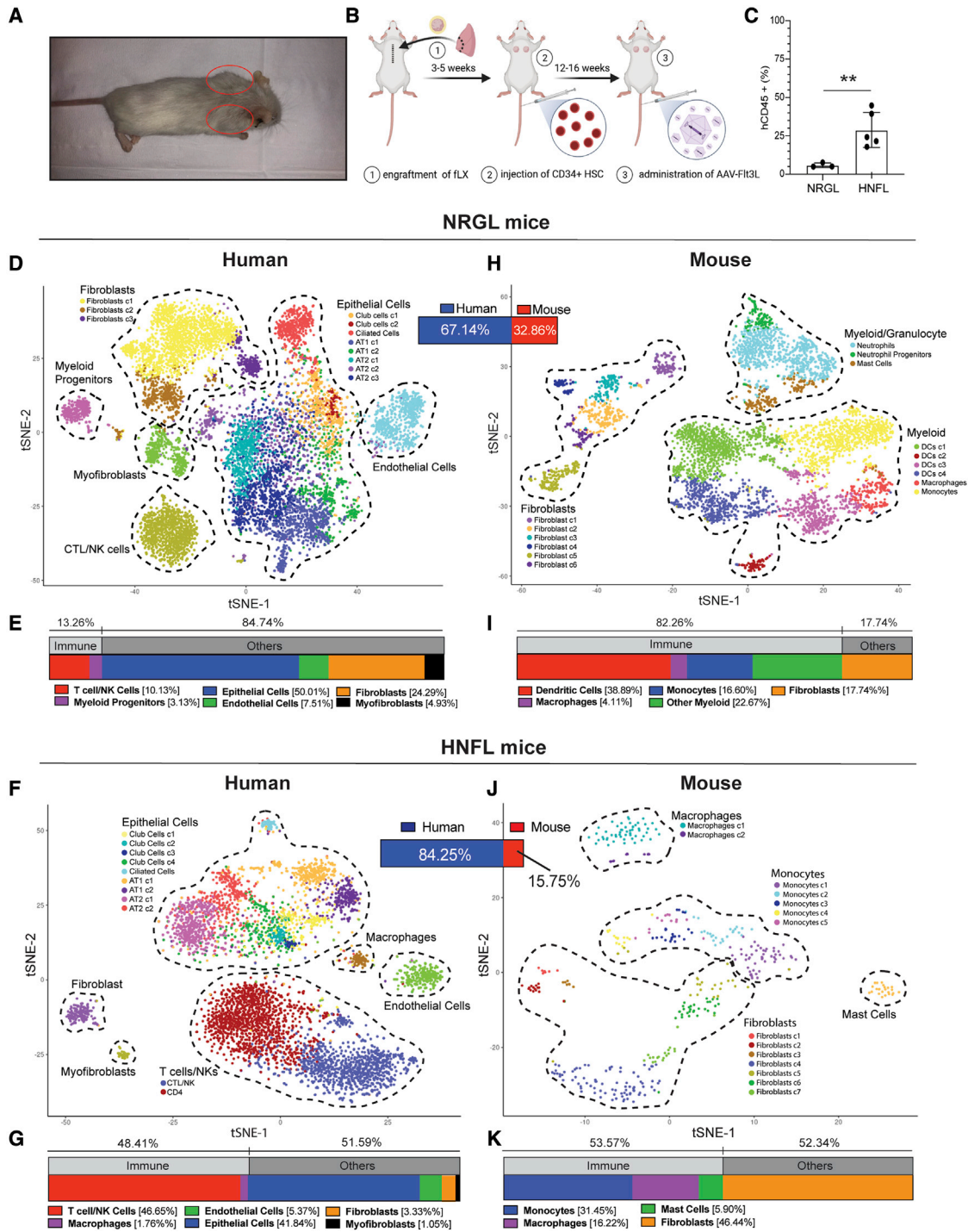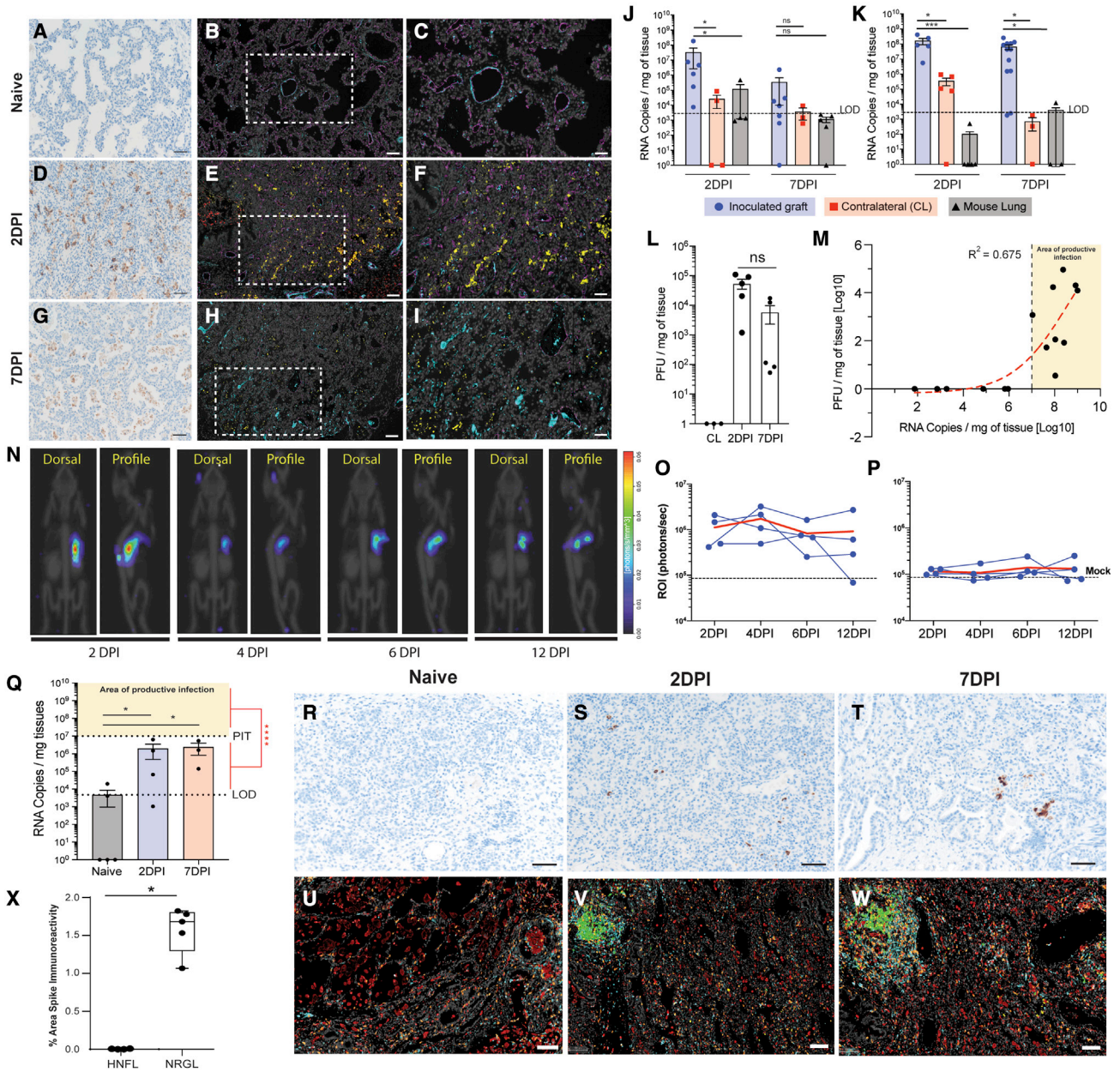
**Figure 1. Generation of HNFL mice**

(A) An NRGL mouse engrafted with pairs of human fLX (red ellipse).

(B) Procedure to generate HNFL mice. Image created with BioRender.com.

(C) Frequency of human CD45+ cells within total CD45+ cells (mouse + human) in naive NRGL-LX and HNFL-LX (flow cytometry analysis). n = 3–5; mean ± SEM; Welch's t test; **p ≤ 0.01.

(D–K) t-distributed stochastic neighbor embedding (t-SNE) plots of the human (D, three fLX, 9,968 cells; F, two fLX, 5,160 cells) and mouse (H, three fLX, 5,091 cells; J, two fLX, 407 cells) compartments in NRGL-LX (D and H) and HNFL-LX (F and J). Relative representation of each species compartment within the fLX is indicated between the two t-SNE plots. Cell subset frequencies (E and G, human; I and K, mouse) are shown below the respective t-SNE plots.

See also Figures S1 and S2; Tables S1 and S2; Video S1.

**Figure 2. HNFL mice are effectively protected from SARS-CoV-2 infection**

(A–I) Representative SARS-CoV-2 N IHC (A, D, G) and five-color IHC (B, C, E, F, H, I; yellow, SARS-CoV-2 Spike; magenta, human CD31; cyan, murine CD61; red, human CD68; gray, DAPI) on naive (A–C) or inoculated NRGL-LX (D–F, 2 DPI; G, H, I, 7 DPI; $10^6$ PFU). (C, F, and I) 2× magnification of the inset located in (B, E, and H), respectively. (B, E, and H) 100×; scale bar, 200 μm; (A, D, and G) 200×; scale bar, 100 μm; (C, F, and I) 400×; scale bar, 50 μm.

(J and K) SARS-CoV-2 viral RNA quantification in inoculated (blue) and contralateral NRGL-LX (red), and in NRGL lung (gray), following infection with $10^4$ (J) or $10^6$ (K) PFU (n = 4–12). Limit of detection (LOD; dotted line) is equivalent to RNA copies/mg tissues in naive fLX (n = 7). Mean ± SEM, Kruskal-Wallis test; *p ≤ 0.05, ***p ≤ 0.001.

(L) Quantification of infectious SARS-CoV-2 particles in contralateral (CL, 7 DPI) or inoculated NRGL-LX (2 and 7 DPI; $10^6$ PFU). n = 3–5 fLX. Mean ± SEM, Kruskal-Wallis test; ns, non-significant.

(M) Non-linear regression between viral RNA copies and PFU per milligram of tissue in inoculated (n = 10; 2 and 7 DPI; $10^6$ PFU), contralateral (n = 3), and naive (n = 2) NRGL-LX. Yellow area represents productive infection. Productive infection threshold (PIT) equal to $10^7$ RNA copies/mg (n = 15).

(N) Representative three-dimensional dorsal and profile views of a single NRGL mouse following inoculation of the right fLX with a SARS-CoV-2 NanoLuc virus ($10^6$ PFU). NanoLuc signal was quantified over 12 days of infection.

(O and P) Regionalized quantification of NanoLuc expression in inoculated (O; n = 4, right fLX; $10^6$ PFU) and contralateral (P; n = 4, left fLX) NRGL-LX over a 12-day course of infection. Mean signal from naive fLX (n = 3) was used to determine assay baseline (mock). Red line represents the mean signal over time.

*(legend continued on next page)*

(Figure S2C). Human T cells and NK cells represented the largest cellular subsets in HNFL-LX (46.65% of all lineages/subsets) (Figure 1G). Strikingly, we detected a fraction of human hematopoietically derived cells in NRGL-LX (13.26%), which was composed of a myeloblast progenitor cluster (c-kit$^+$ SRGN$^+$ CD14$^+$ HPGD$^+$; 3.13%) and a lymphoid cluster with cytotoxic functions (CD8$^+$ T cells and/or NK cells; 10.13%) (Figures 1D and 1E).

The presence of macrophages in HNFL-LX (1.76%; Figures 1F, 1G, and S2D) was a defining characteristic of HNFL mice. Back-to-back proteomic analyses of naive NRGL-LX and HNFL-LX showed significant upregulation of many macrophage markers, such as HCK, SLC9A9, and CD163 (Figure S2E; Table S2) in HNFL-LX. Consistently, quantitative image analysis confirmed a significantly higher engraftment of CD68$^+$ cells in HNFL-LX (Figure S2F). Importantly, the mouse myeloid compartment in HNFL-LX mice was also reduced (15.75%) over NRGL-LX mice (32.86%) (Figures 1H–1K). Altogether, our data show that HNFL-LX are reconstituted with human lymphoid and myeloid lineages and contain a diverse epithelial compartment.

## HNFL mice, but not NRGL mice, are able to effectively control SARS-CoV-2 infection

To examine the susceptibility of NRGL mice to SARS-CoV-2 infection, mice were inoculated with SARS-CoV-2 (USA-WA1/2020 isolate) 10 to 15 weeks post-engraftment via direct intra-fLX inoculation at a viral dose of either $10^4$ or $10^6$ plaque-forming units (PFU). To evaluate the possibility of fLX-to-fLX viral transfer through the peripheral blood, some animals were inoculated only in a single fLX. Non-inoculated fLX from uninfected and infected animals are hereafter referred to as "naive" and "contralateral," respectively. While NRGL mice did not display any signs of clinical disease over the course of infection (Figures S3A–S3C), inoculated fLX displayed gross abnormalities (Figure S3D), which contrasted with a white homogeneous appearance of naive and contralateral fLX.

A dose-dependent immunoreactivity to SARS-CoV-2 nucleocapsid (N) in inoculated fLX was observed (Figures 2A, 2D, 2G, and S3E–S3K). When challenged with $10^6$ PFU, viral antigen was concentrated in pneumocytes and bronchiole epithelium at 2 days post inoculation (DPI) (Figures 2D, S3I, S3J, and S3L), while at 7 DPI antigen was mainly detected in necrotic debris within air spaces (Figures 2G and S3K). Infection appeared to be cleared at 7 DPI for the $10^4$ PFU dose (Figures S2K and S2L). Therefore, we elected to pursue all subsequent experiments using a $10^6$ PFU viral dose. Our findings using a $10^6$ PFU viral dose were supported by five-color fluorescence imaging (DAPI, SARS-CoV-2 Spike, CD31, CD61, CD68) (Figures 2B,

2C, 2E, 2F, 2H, and 2I), which also showed an increase in platelet-rich thrombi in inoculated fLX at 7 DPI, a feature consistent with previous studies in humans and NHPs (Aid et al., 2020; Mackman et al., 2020).

qRT-PCR quantification of viral RNA (E gene) was consistent with immunohistochemistry (IHC) findings (Figures 2J and 2K). Although qRT-PCR suggested that low levels of viral RNA were present in contralateral fLX, SARS-CoV-2 N immunoreactivity was never observed in contralateral fLX (Figure S3M). Infectious viral particles were detected in fLX at both 2 and 7 DPI, supporting evidence of productive infection. No infectious viral particles were recovered from contralateral fLX (Figure 2L), suggesting that a limited amount of viral RNA, but not infectious viral particles, may transfer between fLX through the blood. However, no viral RNA was detected in the peripheral blood at any time point (Figure S3N), suggesting that very low levels of free viral RNA may circulate between fLX. We found a positive non-linear regression between viral load and PFU in inoculated fLX ($R^2$ = 0.675) (Figure 2M) and identified that viral loads in excess of a threshold of $10^7$ RNA copies/mg tissue (i.e., productive infection threshold [PIT]) were indicative of productive infection. Finally, using bioluminescence imaging and a recombinant SARS-CoV-2 expressing NanoLuc luciferase (Xie et al., 2020), we revealed that SARS-CoV-2 replication persisted within single animals for up to 12 DPI (Figures 2N, 2O, and S3O; Video S1) while remaining undetectable in contralateral grafts (Figures 2P and S3O).

In contrast to NRGL mice, intra-fLX inoculation of HNFL mice with SARS-CoV-2 ($10^6$ PFU) resulted in viral RNA copies per milligram of tissues significantly below the PIT (RNA copies/mg < 1 × $10^7$; Figure 2Q) at both 2 and 7 DPI. Consistently, low to no SARS-CoV-2 Spike immunoreactivity was observed as early as 2 DPI in HNFL-LX in comparison with NRGL-LX (Figures 2R–2W). Of note, fLX derived from the same donor were highly susceptible to infection when engrafted in NRG mice (2 DPI, mean = 8.49 × $10^8$ ± 1.29 × $10^8$ RNA copies/mg, n = 3; 7 DPI, mean = 5.50 × $10^8$ ± 1.14 × $10^8$ RNA copies/mg, n = 3). Whole slide quantification of Spike immunoreactivity at 2 DPI confirmed significantly decreased susceptibility of HNFL-LX for SARS-CoV-2 infection (Figure 2X). Notably, we observed the formation of CD20$^+$ B cell lymphoid aggregates in HNFL-LX upon infection (Figures 2V and 2W), suggesting a link between effective control of viral replication and hematopoietic infiltration in HNFL-LX. Of note, fLX engrafted in NRGFL mice (i.e., NRGFL-LX) were equally susceptible to SARS-CoV-2 infection compared with NRGL-LX (Figure S3P), highlighting that the lack of Flk2 expression or a reduced mouse myeloid compartment did not mediate the protective phenotype observed in

(Q) SARS-CoV-2 viral RNA quantification in inoculated HNFL-LX ($10^6$ PFU) at 2 and 7 DPI (n = 3–5 fLX). LOD (dotted line) represents the mean RNA copies/mg tissues in naive fLX (n = 5). Significance between 2 and 7 DPI viral load values and area of productive infection was calculated by running a Kruskal-Wallis test (red line and asterisks) Mean ± SEM; *p ≤ 0.05, ****p ≤ 0.001. PIT, productive infection threshold.

(R–W) Representative SARS-CoV-2 Spike (R, S, T) and six-color IHC (U, V, W; yellow, SARS-CoV-2 Spike; cyan, hCD3e; green, hCD20; orange, hCD8; red, hCD68; gray, DAPI) on naive (R, U) or inoculated ($10^6$ PFU) tissue section (S, V, 2 DPI; T, W, 7 DPI) from HNFL-LX. (R, S, T) 200×; scale bar, 100 μm; (U, V, W) 100×; scale bar, 200 μm.

(X) Quantification of tissue area immunoreactive for SARS-CoV-2 Spike (percentage of analyzed tissue) in inoculated ($10^6$ PFU) HNFL-LX and NRGL-LX (n = 4–5). Mean ± SD, Kolmogorov-Smirnov t test; *p ≤ 0.05.
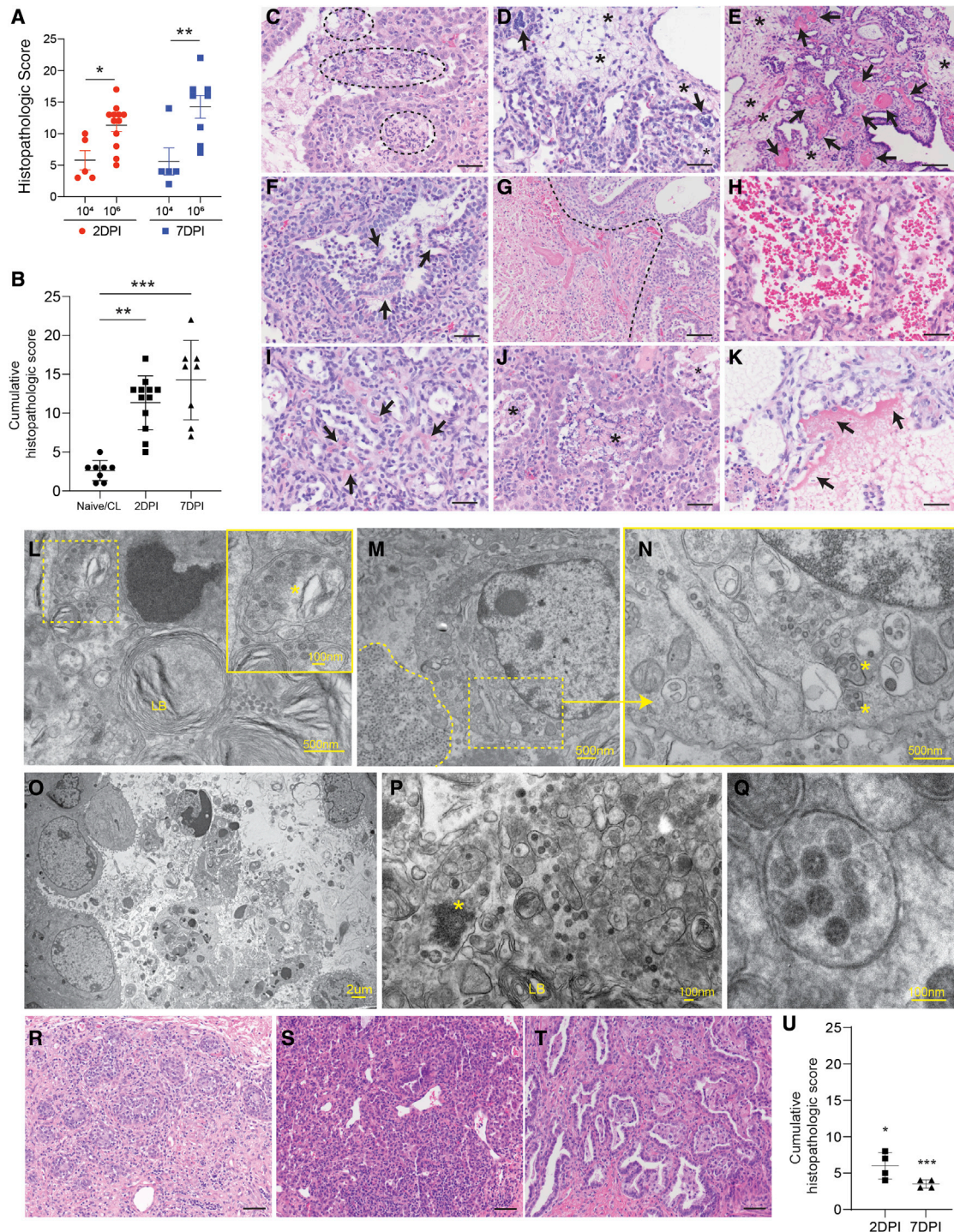
See also Figure S3.

**Figure 3. HNFL mice are protected from severe histopathology**

(A) Cumulative histopathologic score of inoculated NRGL-LX ($10^4$ or $10^6$ PFU) at 2 and 7 DPI (n = 5–10). Mean ± SEM, two-way ANOVA; *p ≤ 0.05, **p ≤ 0.01.

(B) Cumulative histopathologic score of inoculated ($10^6$ PFU; 2 and 7 DPI) and naive/contralateral (CL) NRGL-LX (n = 8–12). Mean ± SEM, Kruskal-Wallis test; **p ≤ 0.01, ***p ≤ 0.001.

(C–K) Representative histopathologic phenotypes of inoculated NRGL-LX ($10^6$ PFU). (C) Neutrophil accumulation within air spaces (within black dashed lines). (D) Syncytial epithelial cells (black arrows) and interstitial edema (asterisks). (E) Fibrin thrombi occluding intermediate-sized blood vessels (black arrows), with interstitial edema (asterisks). (F) Denuded epithelium (black arrows). (G) Coagulative necrosis (left of dashed line), adjacent to viable fLX (right of dashed line).

*(legend continued on next page)*

HNFL mice. Altogether, our data suggest that human hematopoietic engraftment in HNFL mice protects fLX against persistent SARS-CoV-2 infection.

### HNFL mice are protected from histopathological manifestations observed in patients with severe COVID-19

Next, we aimed to probe whether NRGL mice recapitulate histologic phenotypes observed in patients with severe COVID-19 and if HNFL mice are protected against these phenotypes. We developed a semi-quantitative ordinal scoring system based on phenotypes of severe COVID-19 (see STAR Methods). In NRGL-LX, the mean cumulative histologic score in animals inoculated with $10^6$ PFU was 1.76-fold higher at 2 DPI and 2.22-fold higher at 7 DPI compared with those inoculated with $10^4$ PFU, indicating a positive correlation with viral load and SARS-CoV-2 N positivity (Figures 3A and S4A). Of note, tissue integrity and architecture between naive and contralateral fLX were similar, and for this reason both were pooled together to define the histopathological baseline (Figures 3B and S4B). Compared with naive/contralateral fLX, $10^6$ PFU viral inoculation resulted in an increasing histopathological score over time (Figures 3B and S4B). Notably, neutrophil influx, intra-air-space necrosis, capillary fibrin thrombi, and presence of syncytial cells were the most significant independent observations that contributed to the increased cumulative score (Figure S4B). There were no histopathological differences between NRGL-LX and NRGFL-LX at 2 DPI, emphasizing that loss of Flk2 expression does not have an impact on histopathological outcome (Figure S4C).

Histopathologic findings were observed in all SARS-CoV-2-inoculated NRGL-LX, ranging from mild focal to severe generalized disease (Figures 3C–3K), and histologic lesions predominated in areas with SARS-CoV-2 N immunoreactivity. At 2 DPI, affected terminal air spaces were infiltrated by neutrophils (Figure 3C), with variable amounts of edema (Figures 3D and 3E), denuded epithelial cells (Figure 3F), coagulative necrosis (Figure 3G), and hemorrhage (Figure 3H). In areas of severe neutrophilic inflammation, increased numbers of mitotic figures were observed in pneumocytes, supportive of active regeneration (Figure 3C), with concurrent pneumocyte degeneration represented by cytoplasmic swelling and vacuolation. Capillaries and intermediate-sized arterioles and arteries were multifocally occluded by fibrin thrombi (Figures 3E and 3I). Similar features were observed at 7 DPI, but air spaces were more frequently filled with abundant necrotic cellular debris (Figure 3J), and in one fLX, a distinctive hyaline membrane lining pneumocytes could also be observed (Figure 3K). Altogether,

these data demonstrate that SARS-CoV-2 infection of NRGL mice is associated with the development of cellular and histopathological features that resemble those observed in the lungs of patients with severe COVID-19.

Ultrastructural analysis of NRGL-LX inoculated with $10^6$ PFU supported our virological and histopathological findings. Virus particles were observed within AT2 pneumocytes at various stages of maturation and were often confined to double-membrane-bound vesicles (DMVs), with morphology and particle size consistent with previously described coronaviruses (range 80–130 nm in diameter) (Laue et al., 2021) (Figures 3L–3N). Potential single-particle budding events (Figure S4D) were also observed. At 7 DPI, air spaces were filled with abundant necrotic cellular debris, including lamellar bodies, erythrocytes, neutrophils, and denuded viral-particle-containing AT2 pneumocytes (Figures 3O and S4E–S4G), which were occasionally undergoing apoptosis as indicated by the presence of pyknotic nuclei (Figure S4E). DMV-containing viral particles and electron-dense viral replication centers were still observed at 7 DPI, suggesting the persistence of active viral replication (Figures 3P and S4H). Faint Spike protein coronal surface projections were sometimes visible within DMVs (Figure 3Q). Blood vessels also contained aggregates of platelets (Figure S4I) with several small- to intermediate-sized arteries occasionally occluded by fibrin thrombi (Figure S4J).

Consistent with decreased viral loads, cumulative histology scores were significantly decreased in HNFL-LX mice at 2 (p = 0.01) and 7 DPI (p = 0.0002) compared with NRGL-LX (Figures 3R–3U and S4K). HNFL-LX showed decreased syncytial cells and intra-airway necrosis at 2 and 7 DPI, respectively, compared with NRGL-LX. Hemorrhage and influx of neutrophils were also significantly decreased at both 2 and 7 DPI in HNFL-LX but not NRGL-LX (Figure S4K). Taken together, these findings suggest that HNFL mice mount an effective host response in fLX that not only prevents persistent SARS-CoV-2 infection, but also protects from severe histopathological manifestations observed in patients with severe COVID-19.

### Lung tissue protection associates with B cell and macrophage infiltration

We next sought to demonstrate the potential of the HNFL model to capture cellular correlates of protection against SARS-CoV-2. Human CD45+ frequency (Figure 4A) and human lymphoid lineage counts (T cell, B cell, and CD56+ cell; normalized cell counts) significantly increased in HNFL-LX following infection (Figures 4B–4F and S5A). scRNA-seq analysis confirmed

---

(H) Intra-air-space hemorrhage. (I) Fibrin thrombi occluding interstitial capillaries (black arrows). (J) Accumulation of necrotic debris within air spaces (asterisks). (K) Hyaline membrane (black arrows). Hematoxylin and eosin (H&E) staining, 400×, scale bar, 50 μm.

(L–Q) Ultrastructural analysis of inoculated NRGL-L ($10^6$ PFU). (L) SARS-CoV-2 viral particles in double-membrane-bound vesicle (DMV, asterisk) in AT2 pneumocytes (lamellar body, LB) at 2 DPI. Top right corner is a magnification of the top left inset (dotted box). (M) Infected pneumocyte with viral particles around the peripheral extracellular area (left of dashed line) at 2 DPI. (N) Magnification (3.75×) of the inset from (M) with event of viral particle maturation in DMV. (O) Air space filled with necrotic cellular debris, including lamellar bodies and denuded AT2 pneumocytes undergoing apoptosis at 7 DPI. (P) Virus particles at variable stages of maturation within the cytoplasm of AT2 cells at 7 DPI (lamellar bodies, LB). Free and DMV-associated virus particles and electron-dense viral replication centers (asterisk). (Q) Cluster of mature virus particles with radiating spikes and aggregates of nucleocapsid protein contained within a DMV at 7 DPI.

(R–T) Representative H&E staining on naive (R) or inoculated (S, 2 DPI; T, 7 DPI; $10^6$ PFU) HNFL-LX tissue section; 200×, scale bar, 100 μm.

(U) Cumulative histopathologic score of inoculated HNFL-LX ($10^6$ PFU) at 2 and 7 DPI. Mean ± SEM (n = 4). Statistically significant differences with mean cumulative histopathologic score of NRGL-LX (B) at the same time point are indicated with asterisks (two-way ANOVA; *p ≤ 0.05, ***p ≤ 0.001).
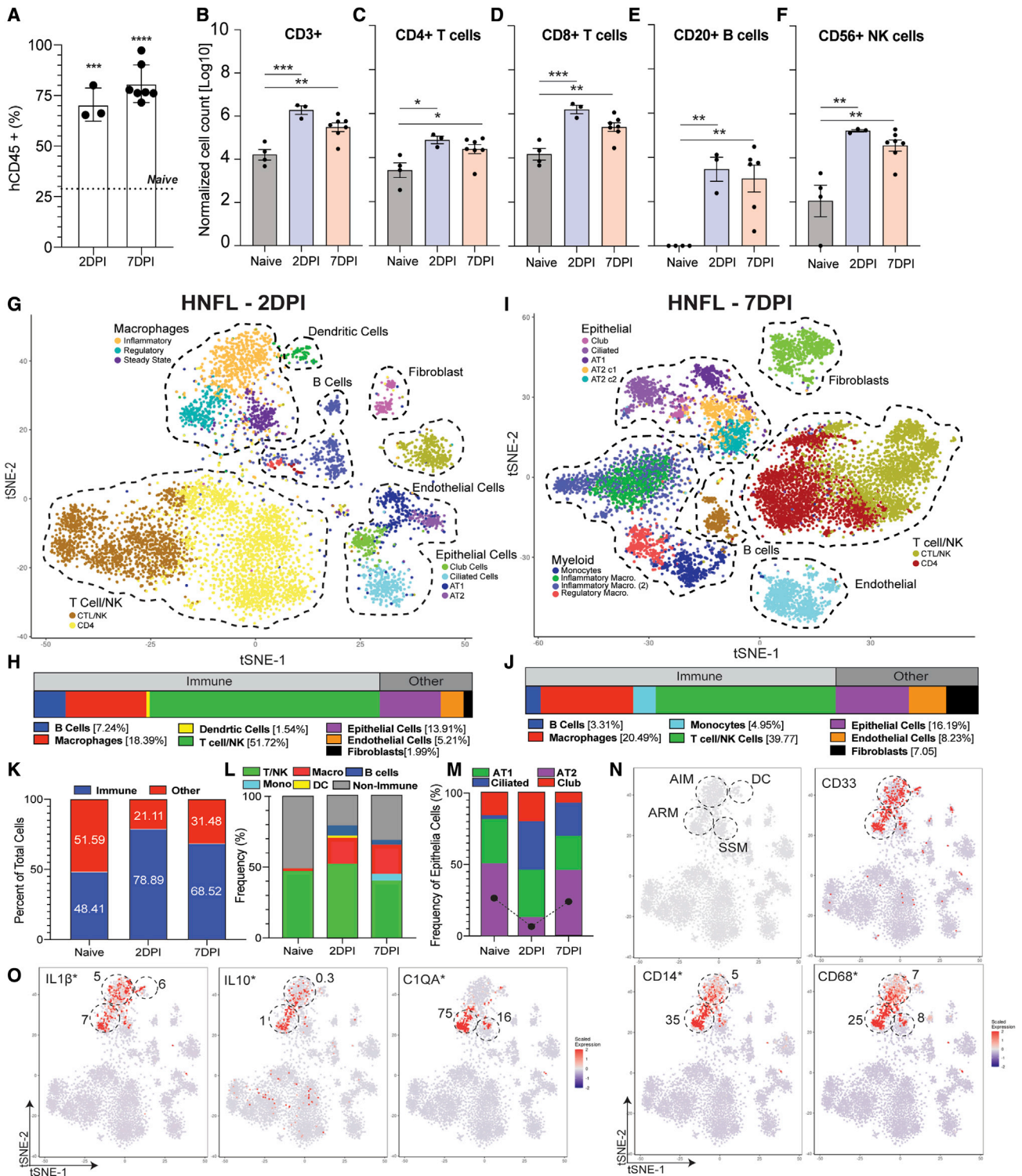
See also Figure S4.

**Figure 4. Infiltration of human hematopoietic lineages in HNFL-LX upon SARS-CoV-2 inoculation**

(A) Frequencies of human CD45$^+$ cells within total CD45$^+$ cells (mouse + human) in HNFL-LX at 2 and 7 DPI (flow cytometric analysis). Dotted line represents mean frequency of CD45$^+$ cells in naive HNFL-LX (Figure 1C) (n = 3–7). Mean ± SEM, one-way ANOVA; ***p ≤ 0.001, ****p ≤ 0.0001 over naive HNFL-LX.

(B–F) Normalized cell count (number of cells analyzed in subset × [total fLX cell count/total cells analyzed]) of hCD3$^+$ T cells (B), hCD3$^+$ hCD4$^+$ T cells (C), hCD3$^+$ hCD8$^+$ T cells (D), hCD20$^+$ cells (E), and hCD3$^-$ hCD20$^-$ hCD33$^-$ hCD56$^+$ cells (F) in naive or inoculated HNFL-LX (2 and 7 DPI) (n = 3–7). Mean ± SEM, one-way ANOVA; *p ≤ 0.05, **p ≤ 0.01, ***p ≤ 0.001.

*(legend continued on next page)*

significant human hematopoietic infiltration in HNFL-LX at 2 DPI (78.89% versus 48.41% in naive fLX) and progressive resorption by 7 DPI (68.52%) (Figures 4G–4L; Table S1). The major subsets mediating hematopoietic expansion were macrophages (naive, 1.76%; 2 DPI, 18.39%; 7 DPI, 20.49%) and B cells (naive, 0%; 2 DPI, 7.24%; 7 DPI, 3.31%) (Figure 4L). B cell infiltration was consistent with flow cytometry (Figure 4E) and six-color imaging data (Figures 2V and 2W). Notably, the frequency of AT2 cells within the epithelial compartment was reduced at 2 DPI (12.7%) but restored at 7 DPI (45.5% versus naive, 50.2%) (Figure 4M), supporting evidence for the successful resolution of infection and progressive restoration of tissue homeostasis.

Focusing on the myeloid compartment, we identified two differentially polarized $CD14^+$ $CD68^+$ activated macrophage subsets at 2 DPI; one had a pro-inflammatory phenotype (herein referred to as activated inflammatory macrophages [AIM]) defined as $CD14^+$ $CD68^+$ $IL-1\beta^+$ and which displayed moderate interferon-stimulated gene (ISG) expression and low IL-10 expression. The other had a regulatory phenotype (subsequently referred to as activated regulatory macrophages [ARM]) defined as $CD14^+$ $CD68^+$ $IL-1\beta^+$ $C1QA^+$ and which displayed high ISG and moderate IL-10 expression (Figures 4N and 4O). Similar macrophage subsets were observed at 7 DPI (Figure S5B). Activated macrophage clusters were significantly associated with moderate expression of several chemokines at 2 DPI, including CCL2–4, CCL8, and CXCL10, which was consistent with monocyte recruitment and macrophage infiltration into fLX upon infection (Table S1). Expression of CCL13 and CCL18, considered to be pro- and anti-inflammatory chemokines, respectively (Mendez-Enriquez and Garcia-Zepeda, 2013; Schraufstatter et al., 2012), was significantly associated with the ARM cluster only, emphasizing the role of ARM as a major regulatory subset.

### Protection from SARS-CoV-2 infection is defined by the upregulation of a subset of 11 genes

We then aimed to capture molecular signatures defining lung tissue protection using a proteomic approach. By analyzing top differentially expressed proteins (33 proteins, log odds $\geq -1$) between inoculated and naive HNFL-LX, we found that HNFL-LX infection was mainly characterized by the induction of a significant type I IFN response and by the upregulation of ISG15, USP18, IFIT1-3, OAS1–3, and MX1–2 at 2 DPI (Figure 5A; Table S2). Through a side-by-side mass spectrometry run and proteomic analysis of both NRGL-LX and HNFL-LX (naive and

2 DPI), we identified 13 proteins among the initial 33 proteins that were upregulated in inoculated HNFL-LX but not in inoculated NRGL-LX at 2 DPI (Figures 5B and S6A; Table S2). This included USP18, OAS1–3, ISG20, IFIH1, IFIT2–3, DDX58, IFIT5, IFI44L, HLA-B, and PDLIM1.

Interestingly, the proteomic signature in HNFL-LX was dominated by the upregulation of the USP18-ISG15 axis, unlike NRGL-LX, which did not display any significant USP18 upregulation (Figures 5C and 5D). In line with the function of USP18 as a negative regulator of type I IFN responses, STAT1 was significantly phosphorylated in NRGL-LX, but not in HNFL-LX (Figures 5E and 5F; Table S3). These findings were consistent with recent evidence of enhanced STAT1 phosphorylation in severe COVID-19 cases (Rincon-Arevalo et al., 2021).

To further validate our set of 13 proteins, we also sought to confirm their upregulation at the transcriptomic level in inoculated HNFL-LX. Using scRNA-seq, we pooled all cell clusters together for each HNFL-LX sample and performed a differential gene expression analysis. This analysis supported the induction of a strong ISG response consistent with proteomic data, with ISG15 being the most upregulated transcript at 2 DPI (Figures 5G and 5H). Of the 13 proteins differentially expressed, 11 (~84% overlap) were also significantly upregulated (log2_FC MAST $\geq 0.2$) at the transcriptomic level in inoculated HNFL-LX (2 DPI) in comparison with naive HNFL-LX (Figures 5G–5I). These genes included USP18, OAS1–3, IFIT2–3, DDX58, ISG20, IFI44L, and IFIH1 and were further defined as protection-defining genes (PDGs).

As a side note, SFTPC was the most downregulated transcript at 2 DPI ($-0.9$ log2FC; false discovery rate [FDR] = $4.42 \times 10^{-232}$; Figure 5G), consistent with the reduction in the AT2 compartment we noted above (Figure 4M) and with previous studies reporting a loss of AT2 program/compartment upon SARS-CoV-2 infection (Delorey et al., 2021). At 7 DPI, SFTPC ($-0.5$ log2FC; FDR = $1 \times 10^{-109}$) and many ISGs were found to be returning to naive fLX expression levels (Figure 5H).

Collectively, our findings highlight that viral clearance and tissue protection from SARS-CoV-2 in HNFL mice are associated with the upregulation of a defined genetic signature composed of 11 specific genes.

### PDG upregulation and lung tissue protection associate with limited pro-inflammatory cytokine expression

To better correlate PDG expression with inflammation and severe histopathology, we employed bulk transcriptomic analysis

---

(G–J) t-SNE plots of the human compartment in HNFL-LX at 2 (G, three fLX, 6,736 cells) and 7 DPI (I, three fLX, 11,269 cells). Cell subset frequencies (H, 2 DPI; J, 7 DPI) are shown below the respective t-SNE plots.

(K) Frequencies of the human hematopoietic fraction (immune) within the human cellular compartment in naive (two fLX, 5,160 cells) or inoculated (2 DPI, three fLX, 6,736 cells; 7 DPI, three fLX, 11,269 cells) HNFL-LX.

(L) Frequencies of different human hematopoietic lineages within the human cellular compartment (two fLX, 5,160 cells) in naive or inoculated (2 DPI, three fLX, 6,736 cells; 7 DPI, three fLX, 11,269 cells) HNFL-LX.

(M) Frequencies of AT1 (green), AT2 (purple), ciliated cells (blue), and club cells (red) within the human epithelial compartment in naive (two fLX, 2,159 cells) or inoculated (2 DPI, three fLX, 937 cells; 7 DPI, three fLX, 1,825 cells) HNFL-LX. A dotted line symbolizes the variation in the size of the AT2 compartment upon infection.

(N, O) t-SNE plots displaying clustered and scaled expression of several transcripts coding for myeloid, inflammatory, and regulatory markers in the human compartment of HNFL-LX at 2 DPI. Clusters of interest (dotted circles) are labeled in the top left plot of (N) (AIM, activated inflammatory macrophages; ARM, activated regulatory macrophages; SSM, steady-state macrophages; DC, dendritic cells). Cluster-defining genes are marked by an asterisk, and log2FC values are indicated near the corresponding cluster(s). n = 3 fLX, 6,736 cells.
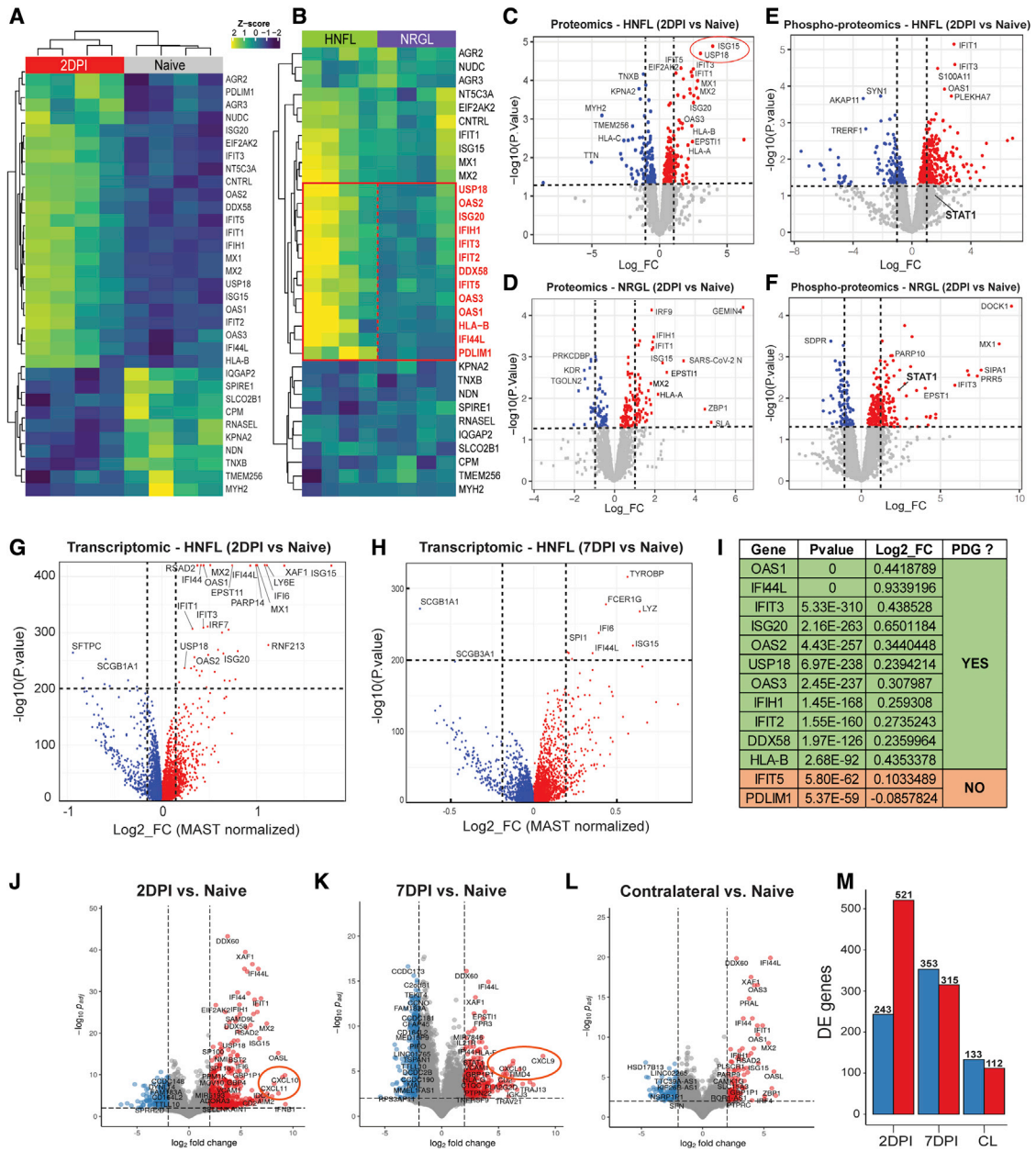
See also Figure S5 and Table S1.

**Figure 5. HNFL mice recapitulate a potent and balanced human antiviral response against SARS-CoV-2 infection**

(A) Cluster heatmap representing the top 33 proteins significantly (p ≤ 0.05) up- (Z > 0) and downregulated (Z < 0) in HNFL-LX at 2 DPI (10^6 PFU, n = 4) in comparison with naive (n = 4) HNFL-LX.

(B) Relative differential expression of the set of 33 selected proteins in HNFL-LX (n = 4) and NRGL-LX (n = 4) at 2 DPI (10^6 PFU) represented through a semi-cluster heatmap. Proteins significantly (p ≤ 0.05) up- (Z > 0) and downregulated (Z < 0) are labeled in red.

(C and D) Differentially expressed proteins in HNFL-LX (C) or NRGL-LX (D) at 2 DPI. Proteins with p ≤ 0.05 (horizontal dashed line) and with logFC ≥ 1 or ≤ −1 (vertical dashed lines) are considered significantly up- or downregulated, respectively. Naive n = 4; 2 DPI n = 4.

(E and F) Differentially phosphorylated proteins at 2 DPI in HNFL-LX (E) and NRGL-LX (F). Proteins with p ≤ 0.05 (horizontal dashed line) and with logFC ≥ 1 or ≤ −1 (vertical dashed lines) are considered significantly up- or downregulated, respectively. Naive n = 4; 2 DPI n = 4.

(G and H) Significantly (p ≤ 0.05) differentially expressed genes (upregulated, red; downregulated, blue) in HNFL-LX at 2 (G) and 7 DPI (H) following infection (10^6 PFU) in comparison with naive HNFL-LX. Fold changes were computed using MAST (Model-based Analysis of Single-Cell Transcriptomics) from pooled scRNA-seq clusters. Transcripts with p ≤ 10^{-200} (horizontal dotted line) and with log2 fold change ≥ 0.2 or ≤ −0.2 (vertical dotted lines) are highlighted. Naive n = 2; 2 DPI n = 3.

(I) List of PDGs found to be upregulated by both proteomics and transcriptomic approaches in inoculated HNFL-LX (YES) or solely via the proteomic approach (NO). Only PDGs found to be upregulated through both approaches were considered as definitive PDGs.

*(legend continued on next page)*

on naive and inoculated NRGL-LX, as mass spectrometry is known to be suboptimal for quantifying cytokine and chemokine expression. Bulk RNA-seq analysis revealed that while NRGL mice mounted a robust type I IFN response at 2 DPI (Figures 5J–5M and S6B–S6F; Table S4), chemokines previously reported to be upregulated in patients with severe COVID-19 (Callahan et al., 2021; Liao et al., 2020; Ren et al., 2021; Wauters et al., 2021), namely, CXCL9, CXCL10, and CXCL11, were among the top 10 upregulated transcripts (Figure 5J). Although IFN responses in inoculated fLX had subsided by 7 DPI (Figures 5K, 5M, S6D, S6E, and S6F), chemokine upregulation remained evident, with CXCL9 ranking as the top most upregulated transcript. Interestingly, evidence of an IFN systemic response was seen in the contralateral graft at 7 DPI (Figures 5L and S6D) despite no evidence of viral replication (Figure 2L). No chemokine mRNAs were upregulated in contralateral grafts (Figure 5L), highlighting a link between viral replication, high chemokine expression, persistent inflammation, and histopathology. A QIAGEN Ingenuity Pathway Analysis (IPA) supported evidence of prolonged inflammation in inoculated but not in contralateral NRGL-LX (Figure S6G), as many processes involving pro-inflammatory cytokines and mediators (IL-2, IL-7, IL-17, chemokine signaling, T cell signaling pathways, etc.) were observed only in inoculated fLX. Notably, IPA suggested a key role for the human resident hematopoietic compartment in these inflammatory processes. No significant transcriptomic signal was detected in the mouse compartment of inoculated NRGL-LX.

In sharp contrast, pooled scRNA-seq transcriptomic analysis of HNFL-LX did not reveal any upregulation of CXCL9-11 at any time points (Figures 5G and 5H), strengthening a potential association between chemokine expression and severe histopathology. No chemokines were among the top upregulated hits (log2FC $\geq$ 0.2 and FDR $\leq$ 1 × 10$^{-200}$) at either 2 or 7 DPI.

Altogether, our data suggest a unique association between PDG upregulation, limited inflammation, and reduced histopathology during SARS-CoV-2 infection of human lung tissues.

### The PDG signature is macrophage enriched

Finally, we aimed to identify the cellular compartment(s) driving PDG upregulation. Using scRNA-seq, we found that our PDG signature was significantly enriched in activated macrophages in comparison with all other cellular compartments at 2 DPI (Figures 6A and 6B; Table S1). Three PDGs (IFIT2, IFIT3, and IFIH1) were also categorized as activated macrophage-defining genes (Figure 6A). Notably, even though it was not identified as a PDG, ISG15 expression was statistically restricted to activated macrophage clusters (Figure 6C), highlighting these clusters as the dominant source of USP18-ISG15 co-expression (Figure 6D). In addition, we found that activated macrophage clusters were the major carriers of viral RNA (p = 0.001), suggesting a potential

association between a dominant macrophage-mediated antiviral response (Figure 6E) and macrophage infection.

Altogether, our findings highlight infiltrating macrophages as a central mediator of the antiviral and anti-inflammatory response at play in HNFL-LX. These data also provide a definitive proof of concept of the potential of HNFL mice to increase our understanding of myeloid immunoregulation defining effective lung tissue protection during SARS-CoV-2 infection.

## DISCUSSION

The pulmonary immunological mechanisms governing protection against SARS-CoV-2 infection remain elusive. To enhance our understanding of these mechanisms, investigations need to go beyond human patient studies due to their inherent limitations.

Here, we report a humanized mouse model, HNFL mice, as an *in vivo* platform enabling the investigation of human myeloid responses in a human lung environment during coronavirus infection. We show that, following SARS-CoV-2 infection, NRGL mice solely engrafted with fLX were highly susceptible to SARS-CoV-2 infection and were prone to severe histopathological manifestations of disease that resemble those observed in patients with severe cases of COVID-19. In sharp contrast, co-engraftment of fLX and human HSCs in HNFL mice resulted in protection against infection, as well as limited histopathology. Infection in HNFL mice was associated with significant hematopoietic infiltration in fLX, as well as with a loss and recovery of the AT2 compartment, demonstrating the ability of the HNFL mice to effectively control infection rather than being resistant to it. Of note, we did not observe any significant signs of human-to-human graft-versus-host disease (GvHD) in fLX, either histologically or by omics analyses. The restoration of the AT2 compartment and the resolution of inflammatory responses toward baseline level at 7 DPI support the notion that the immune signatures observed in fLX were mediated by SARS-CoV-2 infection and not by GvHD.

Protection in HNFL mice was characterized by the upregulation of a macrophage-enriched gene signature composed of 11 genes (USP18, OAS1–3, IFIT2–3, IFIH1, DDX58, HLA-B, IFI44L, and ISG20). The enhanced type I IFN response observed in HNFL-LX was consistent with many patient studies suggesting the importance of a robust type I IFN response to protect from severe COVID-19 (Zhang et al., 2020; Ziegler et al., 2021). An interesting feature of that signature was the HNFL-specific upregulation of USP18 and the enrichment of the USP18-ISG15 axis in activated macrophages, suggesting a potential role of this axis in dampening tissue inflammation during SARS-CoV-2 infection.

Our study proposes a working model (Figure 7) in which lung-resident macrophages in HNFL mice would become locally activated upon detection of SARS-CoV-2 RNA and would promote

---

(J–L) Differentially expressed transcripts in inoculated (J, 2 DPI; K, 7 DPI; 10$^6$ PFU) and contralateral non-inoculated NRGL-LX (L, 7 DPI) in comparison with naive NRGL-LX. Transcripts with p$_{adj}$ $\leq$ 0.05 and with log2 fold change $\geq$ 2 are considered significantly up- (red) or downregulated (blue). Naive n = 3; 2 DPI n = 4; 7 DPI n = 6; CL/contralateral n = 3.

(M) Number of differentially up- (red) or downregulated (blue) genes per time point (2 and 7 DPI) and infection settings (inoculated/CL) in NRGL-LX. Naive n = 3; 2 DPI n = 4; 7 DP n = 6; CL/contralateral n = 3.
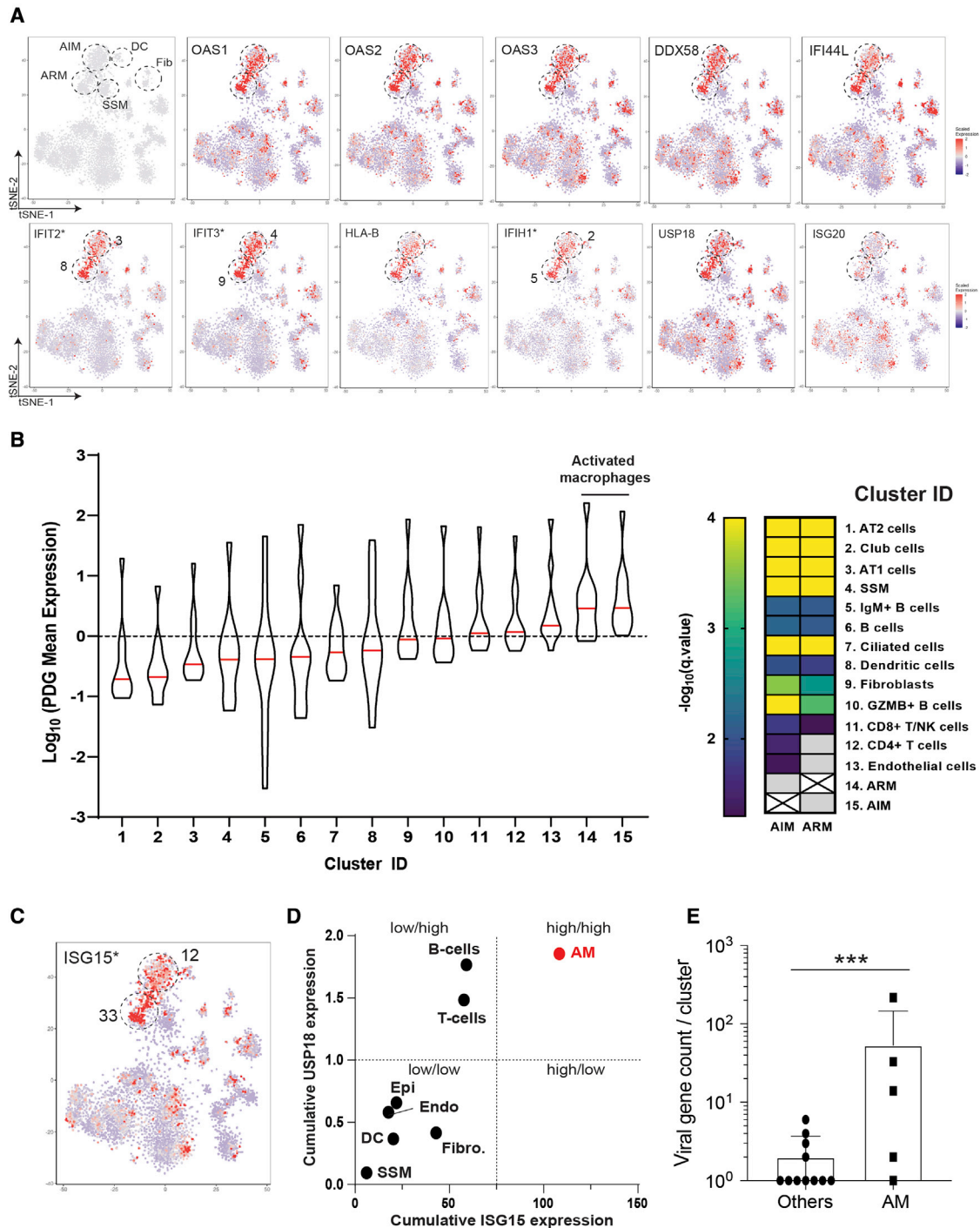
See also Figure S6; Tables S2, S3, and S4.

**Figure 6. Macrophages are the dominant mediators of the antiviral and anti-inflammatory response in HNFL mice**

(A) t-SNE plots displaying clustered and scaled expression of PDG transcripts (OAS1–3, DDX58, IFI44L, IFIT2–3, HLA-B, IFH1, USP18, and ISG20) in the human compartment of HNFL-LX at 2 DPI. Clusters of interest (dotted circles) are labeled in the top left plot. Cluster-defining genes are marked by an asterisk, and log2FC values are indicated near the corresponding cluster; n = 3 fLX, 6,736 cells.

(B) Scaled mean expression of all PDGs in each cluster of the human compartment of HNFL-LX at 2 DPI. For each cluster, the median of the scaled mean expression of all PDGs is shown (red line). Statistically significant differences between combined PDG expression across clusters are reported as a heatmap at the right (RM one-way ANOVA with Geisser-Greenhouse correction). Non-significant differences ($p \geq -\log10[0.05]$) are shown in gray.

*(legend continued on next page)*

monocyte infiltration via regulated secretion of specific inflammatory chemokines (CCL2/4/8, CXCL10). Monocyte infiltration would be followed by macrophage differentiation, activation, and polarization toward inflammatory and regulatory phenotypes. These two subsets of macrophages would then promote a systemic antiviral state across the epithelial compartment in a coordinated fashion, enabling rapid suppression of viral spread and replication. USP18 upregulation, and its increased stabilization through ISG15 interaction, would prevent an excessive inflammatory response by macrophages and protect the tissues from severe histopathological damages.

In contrast, the pro-inflammatory response mediated by tissue-resident human macrophages in NRGL mice following detection of viral RNA would remain a "call in the dark," as the absence of human hematopoietic engraftment in NRGL mice precludes the possibility of any human monocyte recruitment into the fLX. This would therefore prevent the induction of a stronger, systemic antiviral response that could rapidly and effectively clear infection. In addition, the absence of infiltrating macrophages would allow the initial inflammatory response to go unhindered between the resident human lymphoid and myeloid compartments of the fLX, promoting diffuse alveolar damage while further dampening effective antiviral responses. This model is supported by our observation that virus-free contralateral NRGL-LX did not display any histopathological manifestations of disease or prolonged inflammation while mounting a robust type I IFN response. As excessive macrophage-mediated pro-inflammatory responses have been hypothesized to be an important driver of COVID-19 disease progression (Grant et al., 2021; Merad and Martin, 2020; Munnur et al., 2021; Rendeiro et al., 2021; Wauters et al., 2021), it is conceivable that the human macrophage-mediated prolonged inflammation, and/or the absence of effective regulation of inflammation by infiltrating macrophages in NRGL mice, acts as a surrogate of the immunological dysregulations observed in patients with severe COVID-19.

USP18 is the main ISG15 isopeptidase and can repress the establishment of an antiviral state via inhibition of ISG15-mediated ISGylation (Honke et al., 2016; Ketscher et al., 2015). However, USP18 can also directly inhibit type I IFN signaling by binding to STAT2 (Arimoto et al., 2017) and IFNAR2 (Malakhova et al., 2006). Most importantly, ISG15 is a crucial partner to USP18 in this process (Zhang et al., 2015) through its ability to stabilize USP18 and prevent its proteasomal degradation. SARS-CoV-2 infection of macrophages was recently reported to induce papain-like protease protein (PLpro)-mediated de-ISGylation and excessive release of free ISG15 (Munnur et al., 2021). While SARS-CoV-2 infection remains abortive in macrophages

(Boumaza et al., 2021; Yang et al., 2020a; Zheng et al., 2021), such mechanism has been proposed to exacerbate the pro-inflammatory response and "cytokine storm" observed in patients with severe COVID-19. Upregulation of USP18 in infected HNFL-LX could therefore contribute to the maintenance of a positive inflammatory feedback loop through enhanced sequestration of free ISG15 and increased USP18 stabilization. More investigations will be needed to comprehensively delineate the association between limited USP18 expression in macrophages and severe lung inflammation during SARS-CoV-2 infection. The human-specific nature of the USP18-ISG15 interaction positions the HNFL model as a unique resource for such an endeavor.

In summary, our work highlights the remarkable potential of the humanized HNFL mouse model to investigate myeloid correlates of protection from SARS-CoV-2 infection *in vivo* and in a human context. This mouse model, and its future refinements, opens avenues for a better understanding of the immunological mechanisms driving susceptibility to COVID-19 and other viral respiratory diseases and provides a path toward the identification of innovative treatment strategies against these infections.

## Limitations of the study

One limitation of our study involves the lack of evidence that human patients protected from severe COVID-19 also display an upregulated PDG signature in their lung macrophages in contrast to severe COVID-19 cases. However, even though the comparison remains imperfect, combined PDG expression in lung monocytes and macrophages derived from lung autopsy samples of patients with severe COVID-19 (using previously reported datasets; Delorey et al., 2021) was significantly lower than in activated macrophages from infected HNFL-LX (Figure S7), supporting PDG upregulation in macrophages as marker of lung tissue protection.

Another weakness of our study relates to the limited number of human donors used. As this is a clear limitation in comparison with human studies, future humanized mouse studies will have to make every effort to increase intraindividual diversity within cohorts. Finally, direct SARS-CoV-2 inoculation into subcutaneous fetal lung tissues, which do not recapitulate neither the function nor the level of maturation of the human adult lung, also constitutes a limitation of our work. While direct injection within subcutaneous xenografts is a required trade-off for working with human lung tissue *in vivo*, the well-defined compartmentalization of the fLX from the rest of the mouse, their easy access from live animals, and their connection to the vascular system highlight how amenable the NRGL and HNFL models are to investigating host-pathogen interactions during viral respiratory infection. That being said, it is likely that engraftment of human

---

(C) t-SNE plot displaying clustered and scaled expression of ISG15 in the human compartment of HNFL-LX at 2 DPI. Clusters of interest (dotted circles) are labeled in the top left plot of (A). Asterisk indicates that ISG15 is an activated macrophage-defining gene, and log2FC values are indicated near the corresponding cluster; n = 3 fLX, 6,736 cells.

(D) Differential co-expression of the USP18-ISG15 axis across human lineages in inoculated HNFL-LX. Cumulative scaled expression of USP18 and ISG15 was calculated for all human clusters regrouped as specific lineages in HNFL-LX at 2 DPI and plotted on a x/y axis with x and y corresponding to ISG15 and USP18 expression, respectively. Four categories of co-expression were identified and are delineated by dashed lines.

(E) Viral gene count per cluster, segregated between activated macrophage clusters (AM) and all others (Others) in inoculated HNFL-LX (2 and 7 DPI) (n = 29 clusters). Mean ± SD, Mann-Whitney t test, ***p ≤ 0.001. AIM, activated inflammatory macrophages; ARM, activated regulatory macrophages; Epi, epithelial cells; Endo, endothelial cells; SSM, steady-state macrophages; DC, dendritic cells; Fib/Fibro, fibroblasts.
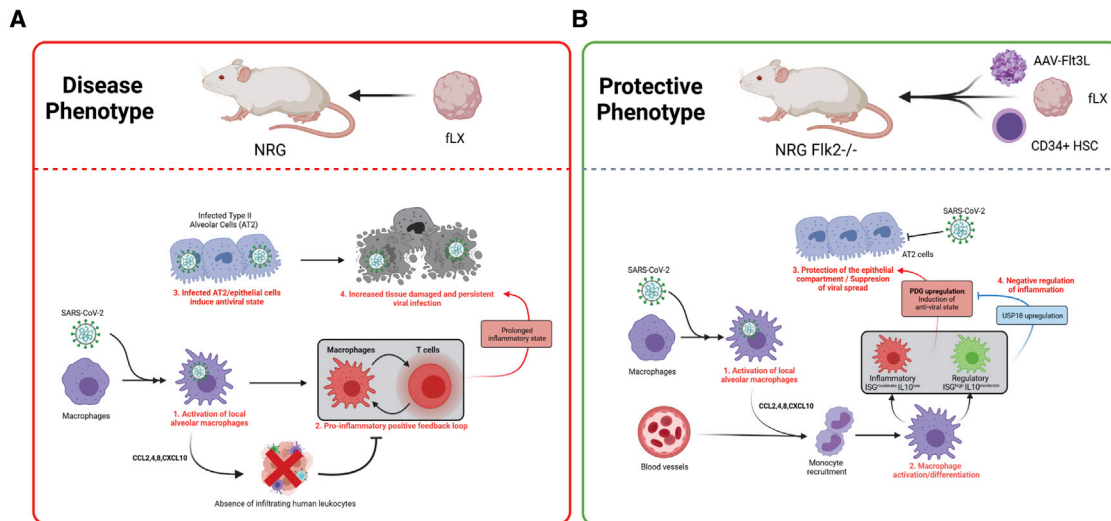
**Figure 7. The HNFL mouse model to uncover myeloid-mediated mechanisms of lung tissue protection during SARS-CoV-2 infection**
(A and B) Working model depicting the cellular and molecular mechanisms that may drive pathology and protection in inoculated HNFL-LX and NRGL-LX, respectively. Image created with BioRender.com.

adult lung tissues over fetal tissues could enhance the potential and biological significance of the HNFL mouse model.

## STAR★METHODS

Detailed methods are provided in the online version of this paper and include the following:

- KEY RESOURCES TABLE
- RESOURCE AVAILABILITY
  - Lead contact
  - Materials availability
  - Data and code availability
- EXPERIMENTAL MODEL AND SUBJECT DETAILS
  - Cell lines
  - Mouse strains
  - Human fetal tissues
- METHOD DETAILS
  - Animal work
  - Virus
  - Tissue processing
  - RNA extraction
  - Flow cytometry
  - Viral quantification
  - Histology and microscopy
  - Proteomics and transcriptomic analysis
  - *In vivo* imaging and data analysis
- QUANTIFICATION AND STATISTICAL ANALYSIS

### SUPPLEMENTAL INFORMATION

Supplemental information can be found online at https://doi.org/10.1016/j.celrep.2022.110714.

### AUTHOR CONTRIBUTIONS

D.K. and F.D. conceptualized the study. D.K., A.K.O., J.T., P.M., R.M.H., T.T., J.H.C., A.E., N.A.C., A.P., and F.D. designed the experiments. D.K., A.K.O., J.T., P.M., R.M.H., T.T., A.R.B., T.R.C., B.B., S.I.G., B.L.H., H.P.G., A.T., A.J.T., E.C., E.T.N., C.M., A.E.T., A.S., S.K., K.G., M.S., A.B.B., N.A.C., A.P., and F.D. performed experiments. D.K., A.K.O., J.T., P.M., R.M.H., T.T., S.A.A., B.B., E.B., M.E., M.S., K.P.F., A.K., N.P., J.D.C., J.H.C., A.E., N.A.C., A.P., and F.D. analyzed the data. J.T., R.M.H., S.A.A., and J.D.C. carried out

computational analysis. K.P.F., A.K., and N.P. carried out bioluminescence imaging analysis. M.E. carried out electron microscopy analysis. B.R.H., M.B., K.P.F., A.K., and N.P provided access to key resources. E.B., M.B., M.E., M.S., K.P.F., A.K., and N.P. provided conceptual and technical inputs and/or helped with data interpretation. D.K., N.A.C., A.P., and F.D. wrote the manuscript with contributions from all authors.

## REFERENCES

Aid, M., Busman-Sahay, K., Vidal, S.J., Maliga, Z., Bondoc, S., Starke, C., Terry, M., Jacobson, C.A., Wrijil, L., Ducat, S., et al. (2020). Vascular disease and thrombosis in SARS-CoV-2-infected rhesus macaques. Cell *183*, 1354–1366.e13.

Andrews, S. (2010). FastQC: A Quality Control Tool for High Throughput Sequence Data. http://www.bioinformatics.babraham.ac.uk/projects/fastqc/.

Arimoto, K.I., Lochte, S., Stoner, S.A., Burkart, C., Zhang, Y., Miyauchi, S., Wilmes, S., Fan, J.B., Heinisch, J.J., Li, Z., et al. (2017). STAT2 is an essential adaptor in USP18-mediated suppression of type I interferon signaling. Nat. Struct. Mol. Biol. *24*, 279–289.

Bastard, P., Rosen, L.B., Zhang, Q., Michailidis, E., Hoffmann, H.H., Zhang, Y., Dorgham, K., Philippot, Q., Rosain, J., Beziat, V., et al. (2020). Autoantibodies against type I IFNs in patients with life-threatening COVID-19. Science *370*, eabd4585.

Basters, A., Knobeloch, K.P., and Fritz, G. (2018). USP18-a multifunctional component in the interferon response. Biosci. Rep. *38*, BSR20180250.

Boumaza, A., Gay, L., Mezouar, S., Bestion, E., Diallo, A.B., Michel, M., Desnues, B., Raoult, D., La Scola, B., Halfon, P., et al. (2021). Monocytes and macrophages, targets of severe acute respiratory syndrome coronavirus 2: the clue for coronavirus disease 2019 immunoparalysis. J. Infect. Dis. *224*, 395–406.

Callahan, V., Hawks, S., Crawford, M.A., Lehman, C.W., Morrison, H.A., Ivester, H.M., Akhrymuk, I., Boghdeh, N., Flor, R., Finkielstein, C.V., et al. (2021). The pro-inflammatory chemokines CXCL9, CXCL10 and CXCL11 are upregulated following SARS-CoV-2 infection in an AKT-dependent manner. Viruses *13*, 1062.

Combes, A.J., Courau, T., Kuhn, N.F., Hu, K.H., Ray, A., Chen, W.S., Chew, N.W., Cleary, S.J., Kushnoor, D., Reeder, G.C., et al. (2021). Global absence and targeting of protective immune states in severe COVID-19. Nature *591*, 124–130.

Delorey, T.M., Ziegler, C.G.K., Heimberg, G., Normand, R., Yang, Y., Segerstolpe, A., Abbondanza, D., Fleming, S.J., Subramanian, A., Montoro, D.T., et al. (2021). COVID-19 tissue atlases reveal SARS-CoV-2 pathology and cellular targets. Nature *595*, 107–113.

Dobin, A., Davis, C.A., Schlesinger, F., Drenkow, J., Zaleski, C., Jha, S., Batut, P., Chaisson, M., and Gingeras, T.R. (2013). STAR: ultrafast universal RNA-seq aligner. Bioinformatics. *29*, 15–21.

Douam, F., and Ploss, A. (2018). The use of humanized mice for studies of viral pathogenesis and immunity. Curr. Opin. Virol. *29*, 62–71.

Douam, F., Ziegler, C.G.K., Hrebikova, G., Fant, B., Leach, R., Parsons, L., Wang, W., Gaska, J.M., Winer, B.Y., Heller, B., et al. (2018). Selective expansion of myeloid and NK cells in humanized mice yields human-like vaccine responses. Nat. Commun. *9*, 5031.

Dudek, T.E., No, D.C., Seung, E., Vrbanac, V.D., Fadda, L., Bhoumik, P., Boutwell, C.L., Power, K.A., Gladden, A.D., Battis, L., et al. (2012). Rapid evolution of HIV-1 to functional CD8(+) T cell responses in humanized BLT mice. Sci. Transl. Med. *4*, 143ra198.

Elias, J.E., and Gygi, S.P. (2007). Target-decoy search strategy for increased confidence in large-scale protein identifications by mass spectrometry. Nat Methods. *4*, 207–214.

Ewels, P., Magnusson, M., Lundin, S., and Käller, M. (2016). MultiQC: summarize analysis results for multiple tools and samples in a single report. Bioinformatics. *32*, 3047–3048.

Finak, G., McDavid, A., Yajima, M., Deng, J., Gersuk, V., Shalek, A.K., Slichter, C.K., Miller, H.W., McElrath, M.J., Prlic, M., et al. (2015). MAST: a flexible statistical framework for assessing transcriptional changes and characterizing heterogeneity in single-cell RNA sequencing data. Genome Biol. *16*, 278.

Frias-Staheli, N., Dorner, M., Marukian, S., Billerbeck, E., Labitt, R.N., Rice, C.M., and Ploss, A. (2014). Utility of humanized BLT mice for analysis of dengue virus infection and antiviral drug testing. J. Virol. *88*, 2205–2218.

Grant, R.A., Morales-Nebreda, L., Markov, N.S., Swaminathan, S., Querrey, M., Guzman, E.R., Abbott, D.A., Donnelly, H.K., Donayre, A., Goldberg, I.A., et al. (2021). Circuits between infected macrophages and T cells in SARS-CoV-2 pneumonia. Nature *590*, 635–641.

Hadjadj, J., Yatim, N., Barnabei, L., Corneau, A., Boussier, J., Smith, N., Pere, H., Charbit, B., Bondet, V., Chenevier-Gobeaux, C., et al. (2020). Impaired type I interferon activity and inflammatory responses in severe COVID-19 patients. Science *369*, 718–724.

Honke, N., Shaabani, N., Zhang, D.E., Hardt, C., and Lang, K.S. (2016). Multiple functions of USP18. Cell Death Dis. *7*, e2444.

Ketscher, L., Hannss, R., Morales, D.J., Basters, A., Guerra, S., Goldmann, T., Hausmann, A., Prinz, M., Naumann, R., Pekosz, A., et al. (2015). Selective inactivation of USP18 isopeptidase activity in vivo enhances ISG15 conjugation and viral resistance. Proc. Natl. Acad. Sci. U S A *112*, 1577–1582.

Kim, Y.I., Kim, S.G., Kim, S.M., Kim, E.H., Park, S.J., Yu, K.M., Chang, J.H., Kim, E.J., Lee, S., Casel, M.A.B., et al. (2020). Infection and rapid transmission of SARS-CoV-2 in ferrets. Cell Host Microbe *27*, 704–709.e2.

Kramer, A., Green, J., Pollard, J., Jr., and Tugendreich, S. (2014). Causal analysis approaches in ingenuity pathway analysis. Bioinformatics *30*, 523–530.

Laue, M., Kauter, A., Hoffmann, T., Moller, L., Michel, J., and Nitsche, A. (2021). Morphometry of SARS-CoV and SARS-CoV-2 particles in ultrathin plastic sections of infected Vero cell cultures. Sci. Rep. *11*, 3515.

Leutert, M., Rodriguez-Mias, R.A., Fukuda, N.K., and Villen, J. (2019). R2-P2 rapid-robotic phosphoproteomics enables multidimensional cell signaling studies. Mol. Syst. Biol. *15*, e9021.

Liao, M., Liu, Y., Yuan, J., Wen, Y., Xu, G., Zhao, J., Cheng, L., Li, J., Wang, X., Wang, F., et al. (2020). Single-cell landscape of bronchoalveolar immune cells in patients with COVID-19. Nat. Med. *26*, 842–844.

Liao, Y., Smyth, G.K., and Shi, W. (2014). featureCounts: an efficient general purpose program for assigning sequence reads to genomic features. Bioinformatics *30*, 923–930.

Love, M.I., Huber, W., and Anders, S. (2014). Moderated estimation of fold change and dispersion for RNA-seq data with DESeq2. Genome biol. *15*, 550.

Mackman, N., Antoniak, S., Wolberg, A.S., Kasthuri, R., and Key, N.S. (2020). Coagulation abnormalities and thrombosis in patients infected with SARS-CoV-2 and other pandemic viruses. Arterioscler. Thromb. Vasc. Biol. *40*, 2033–2044.

Malakhova, O.A., Kim, K.I., Luo, J.K., Zou, W., Kumar, K.G., Fuchs, S.Y., Shuai, K., and Zhang, D.E. (2006). UBP43 is a novel regulator of interferon signaling independent of its ISG15 isopeptidase activity. EMBO J. *25*, 2358–2367.

McCray, P.B., Jr., Pewe, L., Wohlford-Lenane, C., Hickey, M., Manzel, L., Shi, L., Netland, J., Jia, H.P., Halabi, C., Sigmund, C.D., et al. (2007). Lethal infection of K18-hACE2 mice infected with severe acute respiratory syndrome coronavirus. J. Virol. *81*, 813–821.

Mendez-Enriquez, E., and Garcia-Zepeda, E.A. (2013). The multiple faces of CCL13 in immunity and inflammation. Inflammopharmacology *21*, 397–406.

Merad, M., and Martin, J.C. (2020). Pathological inflammation in patients with COVID-19: a key role for monocytes and macrophages. Nat. Rev. Immunol. *20*, 355–362.

Mestas, J., and Hughes, C.C. (2004). Of mice and not men: differences between mouse and human immunology. J. Immunol. *172*, 2731–2738.

Munnur, D., Teo, Q., Eggermont, D., Lee, H.H.Y., Thery, F., Ho, J., van Leur, S.W., Ng, W.W.S., Siu, L.Y.L., Beling, A., et al. (2021). Altered ISGylation drives aberrant macrophage-dependent immune responses during SARS-CoV-2 infection. Nat. Immunol. *22*, 1416–1427.

Perez-Riverol, Y., Csordas, A., Bai, J., Bernal-Llinares, M., Hewapathirana, S., Kundu, D.J., Inuganti, A., Griss, J., Mayer, G., Eisenacher, M., et al. (2019). The PRIDE database and related tools and resources in 2019: improving support for quantification data. Nucleic Acids Res. *47*, D442–D450.

Ren, X., Wen, W., Fan, X., Hou, W., Su, B., Cai, P., Li, J., Liu, Y., Tang, F., Zhang, F., et al. (2021). COVID-19 immune features revealed by a large-scale single-cell transcriptome atlas. Cell *184*, 1895–1913.e19.

Rendeiro, A.F., Ravichandran, H., Bram, Y., Chandar, V., Kim, J., Meydan, C., Park, J., Foox, J., Hether, T., Warren, S., et al. (2021). The spatial landscape of lung pathology during COVID-19 progression. Nature *593*, 564–569.

Rincon-Arevalo, H., Aue, A., Ritter, J., Szelinski, F., Khadzhynov, D., Zickler, D., Stefanski, L., Lino, A.C., Körper, S., Eckardt, K.-U., et al. (2021). Altered increase in STAT1 expression and phosphorylation in severe COVID-19. Preprint at medRxiv. https://doi.org/10.1002/eji.202149575.

Schraufstatter, I.U., Zhao, M., Khaldoyanidi, S.K., and Discipio, R.G. (2012). The chemokine CCL18 causes maturation of cultured monocytes to macrophages in the M2 spectrum. Immunology *135*, 287–298.

Sia, S.F., Yan, L.M., Chin, A.W.H., Fung, K., Choy, K.T., Wong, A.Y.L., Kaewpreedee, P., Perera, R., Poon, L.L.M., Nicholls, J.M., et al. (2020). Pathogenesis and transmission of SARS-CoV-2 in golden hamsters. Nature *583*, 834–838.

Singh, D.K., Singh, B., Ganatra, S.R., Gazi, M., Cole, J., Thippeshappa, R., Alfson, K.J., Clemmons, E., Gonzalez, O., Escobedo, R., et al. (2021). Responses to acute infection with SARS-CoV-2 in the lungs of rhesus macaques, baboons and marmosets. Nat. Microbiol. *6*, 73–86.

Tostanoski, L.H., Wegmann, F., Martinot, A.J., Loos, C., McMahan, K., Mercado, N.B., Yu, J., Chan, C.N., Bondoc, S., Starke, C.E., et al. (2020). Ad26 vaccine protects against SARS-CoV-2 severe clinical disease in hamsters. Nat. Med. *26*, 1694–1700.

Vogel, A.B., Kanevsky, I., Che, Y., Swanson, K.A., Muik, A., Vormehr, M., Kranz, L.M., Walzer, K.C., Hein, S., Guler, A., et al. (2021). BNT162b vaccines protect rhesus macaques from SARS-CoV-2. Nature *592*, 283–289.

Wahl, A., De, C., Abad Fernandez, M., Lenarcic, E.M., Xu, Y., Cockrell, A.S., Cleary, R.A., Johnson, C.E., Schramm, N.J., Rank, L.M., et al. (2019). Precision mouse models with expanded tropism for human pathogens. Nat. Biotechnol. *37*, 1163–1173.

Wahl, A., Gralinski, L.E., Johnson, C.E., Yao, W., Kovarova, M., Dinnon, K.H., 3rd, Liu, H., Madden, V.J., Krzystek, H.M., De, C., et al. (2021). SARS-CoV-2 infection is effectively treated and prevented by EIDD-2801. Nature *591*, 451–457.

Wang, L.X., Kang, G., Kumar, P., Lu, W., Li, Y., Zhou, Y., Li, Q., and Wood, C. (2014). Humanized-BLT mouse model of Kaposi's sarcoma-associated herpesvirus infection. Proc. Natl. Acad. Sci. U S A *111*, 3146–3151.

Wang, Z., Yang, S., Koga, Y., Corbett, S.E., Johnson, E., Yajima, M., and Campbell, J.D. (2020). Celda: a Bayesian model to perform bi-clustering of genes into modules and cells into subpopulations using single-cell RNA-seq data. Preprint at bioRxiv. https://doi.org/10.1101/2020.11.16.373274.

Wauters, E., Van Mol, P., Garg, A.D., Jansen, S., Van Herck, Y., Vanderbeke, L., Bassez, A., Boeckx, B., Malengier-Devlies, B., Timmerman, A., et al. (2021). Discriminating mild from critical COVID-19 by innate and adaptive immune single-cell profiling of bronchoalveolar lavages. Cell Res. *31*, 272–290.

Winkler, E.S., Bailey, A.L., Kafai, N.M., Nair, S., McCune, B.T., Yu, J., Fox, J.M., Chen, R.E., Earnest, J.T., Keeler, S.P., et al. (2020). SARS-CoV-2 infection of human ACE2-transgenic mice causes severe lung inflammation and impaired function. Nat. Immunol. *21*, 1327–1335.

Xie, X., Muruato, A.E., Zhang, X., Lokugamage, K.G., Fontes-Garfias, C.R., Zou, J., Liu, J., Ren, P., Balakrishnan, M., Cihlar, T., et al. (2020). A nanoluciferase SARS-CoV-2 for rapid neutralization testing and screening of anti-infective drugs for COVID-19. Nat. Commun. *11*, 5214.

Yang, D., Chu, H., Hou, Y., Chai, Y., Shuai, H., Lee, A.C., Zhang, X., Wang, Y., Hu, B., Huang, X., et al. (2020a). Attenuated interferon and proinflammatory response in SARS-CoV-2-infected human dendritic cells is associated with viral antagonism of STAT1 phosphorylation. J. Infect. Dis. *222*, 734–745.

Yang, S., Corbett, S.E., Koga, Y., Wang, Z., Johnson, W.E., Yajima, M., and Campbell, J.D. (2020b). Decontamination of ambient RNA in single-cell RNA-seq with DecontX. Genome Biol. *21*, 57.

Zhang, X., Bogunovic, D., Payelle-Brogard, B., Francois-Newton, V., Speer, S.D., Yuan, C., Volpi, S., Li, Z., Sanal, O., Mansouri, D., et al. (2015). Human intracellular ISG15 prevents interferon-alpha/beta over-amplification and auto-inflammation. Nature *517*, 89–93.

Zhang, Q., Bastard, P., Liu, Z., Le Pen, J., Moncada-Velez, M., Chen, J., Ogishi, M., Sabli, I.K.D., Hodeib, S., Korol, C., et al. (2020). Inborn errors of type I IFN immunity in patients with life-threatening COVID-19. Science *370*, eabd4570.

Zheng, J., Wang, Y., Li, K., Meyerholz, D.K., Allamargot, C., and Perlman, S. (2021). Severe acute respiratory syndrome coronavirus 2-induced immune activation and death of monocyte-derived human macrophages and dendritic cells. J. Infect. Dis. *223*, 785–795.

Zhu, N., Zhang, D., Wang, W., Li, X., Yang, B., Song, J., Zhao, X., Huang, B., Shi, W., Lu, R., et al. (2020). A novel coronavirus from patients with pneumonia in China, 2019. N. Engl. J. Med. *382*, 727–733.

Ziegler, C.G.K., Miao, V.N., Owings, A.H., Navia, A.W., Tang, Y., Bromley, J.D., Lotfy, P., Sloan, M., Laird, H., Williams, H.B., et al. (2021). Impaired local intrinsic immunity to SARS-CoV-2 infection in severe COVID-19. Cell *184*, 4713–4733.e22.

## STAR★METHODS

### KEY RESOURCES TABLE

| REAGENT or RESOURCE | SOURCE | IDENTIFIER |
| --- | --- | --- |
| Antibodies | | |
| mouse monoclonal anti-human HLA-DR [L243] BV510 | BioLegend | 307646; RRID:AB_2561948 |
| mouse monoclonal anti-human CD3 [UCHT1] BV605 | BioLegend | 300460; RRID:AB_2564380 |
| mouse monoclonal anti-human CD20 [2H7] BV650 | BioLegend | 302336; RRID:AB_2563806 |
| mouse monoclonal anti-human CD16 (FCgRIII) [B73.1] BV711 | BioLegend | 360732; RRID:AB_2800992 |
| mouse monoclonal anti-human CD45 [H130] BV785 | BioLegend | 304048; RRID:AB_2563129 |
| mouse monoclonal anti-human CD8a [RPA-T8] FITC | BioLegend | 301006; RRID:AB_314124) |
| mouse monoclonal anti-human CD33 [WM53] PE | BioLegend | 303404; RRID:AB_314348 |
| rat monoclonal anti-mouse CD45 [30-F11] PE-Dazzle5 | BioLegend | 103146; RRID:AB_2564003 |
| mouse monoclonal anti-human CD14 [HCD14] PerCp-Cy5.5 | BioLegend | 325622; RRID:AB_893250 |
| mouse monoclonal anti-human CD45RA [HI100] PE-Cy7 | BioLegend | 304126; RRID:AB_10708879 |
| mouse monoclonal anti-human CD56 [QA17A16] APC | BioLegend | 392406; RRID:AB_2728402 |
| mouse monoclonal anti-human CD4 [SK3] AF700 | BioLegend | 344622; RRID:AB_2563150 |
| FcX | BioLegend | 422302; RRID:AB_2818986 |
| LIVE/DEAD Viability NearIR | ThermoFisher | L10119 |
| mouse monoclonal anti-human CD34 [581] FITC | BD Biosciences | 555821; RRID:AB_396150 |
| mouse monoclonal anti-human CD45 [H130] V500 | BD Biosciences | 560777; RRID:AB_1937324 |
| rat monoclonal anti-mouse CD45 [30-F11] PE-Cy7 | BioLegend | 103114; RRID:AB_312979 |
| mouse monoclonal anti-human CD3 [SK7] FITC | eBioscience | 11-0036-42; RRID:AB_1272072 |
| mouse monoclonal anti-human CD19 [HIB19] APC | eBioscience | 17-0199-42; RRID:AB_10804519 |
| mouse monoclonal anti-human CD8 [G42-8] FITC | BD Biosciences | 551347; RRID:AB_394159 |
| mouse monoclonal anti-human CD56 [HCD56] APC | BioLegend | 318310; RRID:AB_604106 |
| mouse monoclonal anti-human CD33 [WM53] PerCp-Cy5.5 | BioLegend | 983906; RRID:AB_2890878 |
| mouse monoclonal anti-human CD11c [B-LY6] APC | BD Biosciences | 559877; RRID:AB_398680 |
| mouse monoclonal anti-human CD11c [3.9] AF700 | BioLegend | 301648; RRID:AB_2819923 |
| mouse monoclonal anti-human CD123 [6H6] eFluor450 | eBioscience | 48-1239-42; RRID:AB_1548710 |
| mouse monoclonal anti-human CD14 [61D3] PE-eFluor610 | eBioscience | 61-0149-42; RRID:AB_2574534 |
| mouse monoclonal anti-human CD14 [Tuk4] Alexa Fluor 700 | Invitrogen | MHCD1429; RRID:AB_1464887 |
| mouse monoclonal anti-human CD3 [7D6] PE-Cy5.5 | Invitrogen | MHCD0318; RRID:AB_10376001 |
| mouse monoclonal anti-human CD4 [RPA-T4] PE | eBioscience | 12-0049-80; RRID:AB_657745 |
| mouse monoclonal anti-human CD19 [SJ25C1] eFluor450 | eBioscience | 48-0198-42; RRID:AB_11220071 |
| mouse monoclonal anti-human CD16 [3G8] PE-TexasRed | Invitrogen | MHCD1617; RRID:AB_1464937 |
| rabbit polyclonal anti-SARS-CoV Nucleoprotein | Novus Biologicals | 100–56576; RRID:AB_838838 |
| mouse monoclonal anti-SARS-CoV-2 Spike [E7U6O/2B3E5] | Cell Signaling | 52342S |
| rabbit monoclonal anti-human CD31 [JC/70A] | Biocare Medical | CM347A |
| rabbit monoclonal anti-mouse CD31 [D8V9E] | Cell signaling | 77699; RRID:AB_2722705 |
| rabbit monoclonal anti-human ACE2 [EPR34435] | Abcam | ab108252; RRID:AB_10864415 |
| rabbit polyclonal anti-human SFTSPC | Seven Hills Bioreagents | WRAP-9337 |
| mouse monoclonal anti-human CD68 [KP1] | Agilent | M081401-2; RRID:AB_2750584 |
| rabbit monoclonal anti-mouse CD61 [ARC0460] | Invitrogen | MA5-35245; RRID:AB_2849148 |
| rabbit polyclonal anti-human CD3 | Dako | A045201-2 |
| rabbit monoclonal anti-human CD8 [SP57] | Roche | 790–4460; RRID:AB_2335985 |
| mouse monoclonal anti-human CD20 [L26] | Dako | 74332 |
| Opal 480 | Akoya Bioscences | FP1500001KT |

*(Continued on next page)*

*Continued*

| REAGENT or RESOURCE | SOURCE | IDENTIFIER |
|---|---|---|
| Opal 520 | Akoya Biosciences | FP1487001KT |
| Opal 570 | Akoya Biosciences | FP1488001KT |
| Opal 620 | Akoya Biosciences | FP1495001KT |
| Opal 690 | Akoya Biosciences | FP1497001KT |
| DAB chromogen | Roche | 760–159 |
| Purple chromogen | Roche | 760–229 |
| Bacterial and virus strains | | |
| Recombinant Severe Acute Respiratory Syndrome Coronavirus 2 – Nano Luciferase (SARS-CoV-2-NL) | Pei-Yong Shei Laboratory | Xie et al., 2020 |
| Severe Acute Respiratory Syndrome Coronavirus 2 (2019-nCoV/USA-WA1/2020) | BEI | MN985325 |
| Biological samples | | |
| Fetal lung tissues (18–22 weeks) | Advanced Biosciences Resources (ABR) | Alameda, CA |
| Chemicals, peptides, and recombinant proteins | | |
| Penicillin-Streptomycin | GIBCO | 15140122 |
| Dimethyl Sulfoxide (DMSO) | Fisher | D1284 |
| Hank's Balanced Salt Solution (HBSS) | Gibco | 14025134 |
| RNA Later | Sigma-Aldrich | R0901500ML |
| Furimazine, 98% | MedChemExpress | HY-111497 |
| Sucrose | Sigma Aldrich | S0389 |
| Ethylenediaminetetraacetic acid (EDTA) Disodium salt | Fisher | BP120 1 |
| Tris-Base | Fisher | BP152 5 |
| Soduim Chloride (NaCl) | Fisher | S271 3 |
| Avicel PH-591 | Dupont Chemical | N/A |
| Formaldehyde, Buffered, Certified, 10% (v/v) | Fisher | LC146705 |
| Tween-20 10% solution | Teknova | T0710 |
| PacI | New England BioLabs (NEB) | R0547L |
| MluI-HF | New England BioLabs (NEB) | R3198L |
| PEG8000 | Sigma | 81268 |
| Spermine | Sigma | S3256 |
| Benzonase | Sigma | E1014 |
| Iodixanol | Sigma | D1556 |
| Pluronic F-68 | Gibco | 24040032 |
| Glycerol | VWR chemicals BDH | BDH1172-4LP |
| Xylene | Leica | 3803665 |
| Hematoxylin | Leica | 3801575 |
| Eosin | Leica | 3801616 |
| 25% Glutaraldehyde | Electron Microscopy Sciences | 16220 |
| Sodium cacodylate buffer (pH 7.4) | Electron Microscopy Sciences | 15949 |
| Osmium Tetroxide | Electron Microscopy Sciences | 19110 |
| 16% Paraformaldehyde | Electron Microscopy Sciences | 15710 |
| Maleic Acid (pH 5.5) | Electron Microscopy Sciences | 18150 |
| Uranyl Acetate | Electron Microscopy Sciences | 22400 |
| Proplene Oxide | Electron Microscopy Sciences | 20412 |
| TAAB Epon | TAAB | T022 |
| Liberase TM | Roche | 5401127001 |
| DNase I grade II | Sigma | 10104159001 |

*Continued*

| REAGENT or RESOURCE | SOURCE | IDENTIFIER |
|---|---|---|
| **Critical commercial assays** | | |
| Quick-RNA Viral Kit | Zymo Research Corporation | R1035 |
| RNeasy Plus Mini Kit | Qiagen | 74134 |
| On-Column DNase | Qiagen | 79256 |
| Chromium Next GEM Single Cell 3′ GEM, library & Gel Bead Kit v3.1 | 10X Genomics | PN-1000121 |
| Chromium Next GEM Chip G Single Cell Kit | 10X Genomics | PN-1000127 |
| Quanta qScript™ XLT One-Step RT-qPCR ToughMix® | VWR | 76047–082 |
| TMTPro 16plex | ThermoFisher | A44520 |
| AbC Anti-Mouse Bead Kit | ThermoFisher | A-10334 |
| In-Fusion | Takara | 638943 |
| CD34 + HSC isolation kit | Stem Cell Technologies | 17856 |
| Luna® Universal One-Step RT-qPCR Lot | New England BioLabs | E3005E |
| **Deposited data** | | |
| Single cell RNA-seq raw data (NRGL/HNFL mice) | GEO | GSE180063 |
| Bulk RNA-seq (NRGL mice) | GEO | GSE180908 |
| Proteomics/Phosphoproteomics (NRGL mice Naive, 2DPI, 7DPI) | ProteomeXchange | PXD025851 |
| Proteomics/Phosphoproteomics (NRGL Naive/2DPI and HNFL Naive/2DPI) | ProteomeXchange | PXD025851 |
| Supplemental Items | Mendeley Data | https://doi.org/10.17632/jxjg8k4xy2.3 |
| **Experimental models: Cell lines** | | |
| *Chlorocebus sp.*: Vero E6 | N/A | N/A |
| AAV-293 cells | ATCC | N/A |
| **Experimental models: Organisms/strains** | | |
| Mouse: NOD.Cg-*Rag1*$^{tm1Mom}$*Il2rg*$^{tm1Wjl/SzJ}$ | The Jackson Laboratory | 007799 |
| Mouse: NOD.Cg-*Rag1*$^{tm1MomFlt3tm1lrl}$*Il2rg*$^{tm1Wjl/SzJ}$ | The Jackson Laboratory | 033127 |
| Mouse: B6.Cg-Tg(K18-ACE2)2Prlmn/J | The Jackson Laboratory | 34860 |
| **Oligonucleotides** | | |
| Probe E_Sarbeco_P1: FAM-ACACTAGCCATCCTTACTG CGCTTCG-BHQ1 | IDT | 10006892 |
| Primer E_Sarbeco_R2: ATATTGCAGCAGTACGCACACA | IDT | 10006890 |
| Primer E_Sarbeco_F1: ACAGGTACGTTAATAGTTAATAGCGT | IDT | 10006887 |
| Primer for AAV flt3 forward: AGGTCGGTATCCACACTAGTCC ACCCGAGCTCGAATTCCGGG | Eton | N/A |
| Primer for AAV flt3 reverse: CGACGGATCCCCCTAATCATCG ATGAATTCCGGG | Eton | N/A |
| Primer for BGH forward: TAGGGGGATCCGTCGACTAGAG | Eton | N/A |
| Primer for BGH reverse: GCGTGTACACTAGGCGGCCGCGC CATAGAGCCCACCGCATC | Eton | N/A |
| human ACE2 qPCR forward primer: CGAAGCCGAAGACCTG TTCTA | Eton | N/A |
| human ACE2 qPCR reverse primer: GGGCAAGTGTGGACTG TTCC | Eton | N/A |
| human RPS11 qPCR forward primer: TTCAGACTGAGCGTGC CTAC | Eton | N/A |
| human RPS11 qPCR reverse primer: GCCCTCAATAGCCTCCTTGG | Eton | N/A |
| **Recombinant DNA** | | |
| pAB269 AAV backbone – AAV2 ITRs | OHSU, Oregon | Markus Grompe |
| pAL119-FLT3L | Addgene | 21910 |

*(Continued on next page)*

*Continued*

| REAGENT or RESOURCE | SOURCE | IDENTIFIER |
|---|---|---|
| pX602-AAV-TBG::NLS-SaCas9-NLS-HA-OLLAS-bGHpA; U6::Bsal-sgRNA | Addgene | 61593 |
| pAB269-TBG-FLT3 LG-BGH | Princeton University, NJ | Alexander Ploss |
| pXR8 | NGVB | N/A |
| **Software and algorithms** | | |
| FastQC | Andrews, 2010 | v0.11.7 |
| MultiQC | Ewels et al., 2016 | v1.6 |
| featureCounts | Liao et al., 2014 | v1.6.2 |
| STAR | Dobin et al., 2013 | v2.7.1a |
| R | R Core Team, 2020 | v4.0.2 |
| DESeq2 | Love et al., 2014 | v1.28.1 |
| Ingenuity Pathway Analysis (IPA) | Qiagen | v01-20-04 |
| MaxQuant | Max Planck Institute | v.1.6.7.0 |
| CellRanger | 10X Genomics | v3.0.0 |
| InForm | Akoya Biosciences | v2.4.8 |
| HALO | Indica Labs Inc. | v3.3.2541.262 |
| QuantStudio Design and Analysis software | Applied BioSystems | v1.5.1 |
| InVivoAX | In Vivo Analytics | N/A |
| GraphPad Prism | GraphPad softwarem | v9.0.1 |
| FlowJo | Beckon, Dickinson, and Company | v10.7.1 |
| Microsoft Excel | Microsoft | Office 365 |
| Microsoft Word | Microsoft | Office 365 |
| Endnote X9 | Clarivate Analytics | X9.3.3 |
| Adobe Illustrator 2021 | Adobe | v25.0 |
| **Other** | | |
| Dulbecco's Modified Eagle Medium (DMEM) | GIBCO | 11995073 |
| Roswell Park Memorial Institute (RPMI) medium 1640 | GIBCO | 11875119 |
| OpitMEM Reduced Serum Media | GIBCO | 51985034 |
| Phosphate Buffer Saline (PBS) | GIBCO | 14190250 |
| Fetal Bovine Serum (FBS) | Atlanta Biologicals | S11550 A18006 |
| ACK lysing buffer | GIBCO | LSA1049201 |
| Cell Strainer 70uM Sterile | Fisher | 22363548 |
| 5 mm Stainless steel bead | Qiagen | 69989 |
| Mulitvette 600uL EDTA | Sarstedt | 15.1671.100 |
| SPRIselect | Beckman Coulter | B23317 |
| DynaBeads MyOne Silane | Invitrogen | 37002D |
| TE buffer | Invitrogen | 12090015 |
| AccuCheck Counting Beads | Life Tecnologies | PCB100 |
| XBridge Peptide BEH C18 column (130A°, 3.5 mm, 4.6 mm × 250 mm) | Waters Corporation | 186003570 |
| Fe-NTA magnetic beads | CubeBiotech | Leutert et al. (2019) |
| EASY-Spray column | ThermoFisher | ES803A |
| Dapi | Akoya Biosciences | FP1490 |
| Corning Matrigel Basement Membrane Matrix | Corning | 354234 |
| pHelper | Agilent | 240071 |
| Amicon® Ultra-15 (100 MWCO) | Millipore Sigma | UFC910024 |

## RESOURCE AVAILABILITY

### Lead contact

Further information and requests for resources and reagents should be directed to and will be fulfilled by the Lead Contact, Dr. Florian Douam (fdouam@bu.edu).

### Materials availability

All reagents and materials will be made available on request after completion of a Materials Transfer Agreement.

### Data and code availability

- The mass spectrometry proteomics data have been deposited to the ProteomeXchange Consortium via the PRIDE (Perez-Riverol et al., 2019) partner repository with the dataset identifier PXD025851.
- Transcriptomic data from bulk RNA sequencing are available through the National Center for Biotechnology Information Gene Expression Omnibus (GEO) under series accession no. GSE180908.
- Transcriptomic data from single cell RNA sequencing are available through the National Center for Biotechnology Information Gene Expression Omnibus (GEO) under series accession no. GSE180063.
- This paper does not report original code.
- Any additional information required to reanalyze the data reported in this paper is available from the Lead contact author upon request.

## EXPERIMENTAL MODEL AND SUBJECT DETAILS

### Cell lines

VeroE6 cells and AAV-293 cells (ATCC) were grown in Dulbecco's modified Eagle's medium (DMEM) supplemented with 10% heat inactivated fetal bovine serum (Bio-Techne, R&D systems, Minneapolis, MN, USA) and 1% (v/v) Penicillin Streptomycin (Thermo Scientific, Waltham, MA, USA).

### Mouse strains

NOD $Rag1^{-/-}$ $IL2Rg^{null}$ mice (NOD.Cg-$Rag1^{tm1Mom}Il2rg^{tm1Wjl/SzJ}$, were obtained from the Jackson Laboratory, catalog number 007799). NRG-Flk2−/− (NRGF) mice (NOD.Cg-$Rag1^{tm1Mom}$ $Flt3^{tm1Irl}$ $Il2rg^{tm1Wjl}$/J) were generated as described previously (Douam et al., 2018) and are available at The Jackson Laboratory (Bar Harbor, ME, USA) (catalog number 033127). NRG and NRGF mice were maintained at the Laboratory Animal Resource Center at Princeton University prior to engraftment with human tissues and shipment to the NEIDL.

In the NEIDL BSL-3 facility, mice were group-housed by sex in Tecniplast green line individually ventilated cages (Tecniplast, Buguggiate, Italy). Mice were maintained on a 12:12 light cycle at 30–70% humidity and provided sulfatrim-containing water and standard chow diets (LabDiet, St. Louis, MO, USA).

All mice in this study were inoculated with SARS-CoV-2 at an age of 20–30 weeks old. Both male and female mice were used.

### Human fetal tissues

Human fetal livers and lungs were procured from Advanced Bioscience Resources (Alameda, CA, USA). Donor list is available in Table S5.

## METHOD DETAILS

### Animal work

#### Institutional approvals

All animal experiments described in this study were performed in accordance with protocols (number 1930) that were reviewed and approved by the Institutional Animal Care and Use and Committee of Princeton University (#1930) and Boston University (PROTO202000020). All mice were maintained in facilities accredited by the Association for the Assessment and Accreditation of Laboratory Animal Care (AAALAC). All replication-competent SARS-CoV-2 experiments were performed in a biosafety level 3 laboratory (BSL-3) at the Boston University National Emerging Infectious Diseases Laboratories (NEIDL).

#### Generation of mice engrafted with human fetal lung xenografts (fLX)

Fetal lung tissues within a gestational age range of 18–22 weeks were obtained from Advanced Biosciences Resources (Alameda, CA, USA). Upon receipt, fetal lung tissue was trimmed of visible connective tissue before the lung was processed into cubes (3–5 mm/side) and placed into DMEM. NRG and NRGF mice (greater than 6 weeks of age) were anesthetized using isoflurane and placed in prone position. A midline incision was made along the skin of the upper back of the mouse. Forceps were used to create subdermal pockets on either side of the midline incision. A piece of lung was dried on a sterile drape and coated with Corning

(Corning, NY, USA) Matrigel Basement Membrane Matrix (product number 354234). Matrigel-coated lung pieces were inserted into each of the subdermal pockets. Skin clips were used to secure the incision. Mice were used for infections 10–15 weeks following engraftment. Fetal lung xenografts derived from five different donors (ID: 6497, 6522, 6538, 6588 and 7165) were used in this study (See Table S5). To reduce variables, cohorts of HNFL mice were all engrafted with a single fetal lung donor (ID: 6588) but with four different hematopoietic donors (see method section below). A cohort of NRG mice engrafted with that same tissue donor (6588) confirmed the high susceptibility to infection of that tissue donor (when engrafted into an NRG mice). The susceptibility to infection of tissue donor 6588 was similar than the other tissue donors we tested (6497, 6522, 6538, and 7165).

### Isolation of human CD34 + hematopoietic stem cell (HSC)

Human fetal livers (16–22 weeks of gestational age) were procured from Advanced Bioscience Resources. Fetal liver was homogenized and incubated in digestion medium (HBSS with 0.1% collagenase IV (Sigma-Aldrich, Darmstadt, Germany), 40 mM HEPES, 2 M CaCl2 and 2 UU/mL DNAse I (Roche) for 30 min at 37°C. Human CD34 + HSC were isolated using a CD34 + HSC isolation kit (Stem Cell Technologies, Cambridge, MA, USA) according to the manufacturer's protocol. Purification of human CD34 + cells were assessed by flow cytometry using an anti-human CD34-FITC antibody (clone 581, BD Biosciences). Fetal liver derived from four different donors (ID: 6676, 1430, 1477 and 1430) were used in this study (See Table S5).

### Generation of human immune system-engrafted mice

3–5 weeks post fLX engraftment, NRGFL mice were irradiated with 300 cGy and $7$–$10 \times 10^5$ human CD34 + HSC were injected intravenously 4–6 h after irradiation. Male and female mice transplanted with CD34 + HSC derived from three different human donors were used in this study. Twelve weeks post HSC engraftment, peripheral levels of humanization were checked. Mice with peripheral engraftment level >40% were enrolled in the study. One-week prior SARS-CoV-2 infection, NRGFL mice were injected intravenously (tail vein) with $2 \times 10^{11}$ copies of AAV-Flt3LG resuspended in 200 μL of 1X phosphate-buffered saline (PBS) containing 35 nM NaCL, 0.002%pluronic F-68 and 5%glycerol.

### Inoculation of humanized mice by intra-fetal lung xenograft injection with SARS-CoV-2

Ten to fifteen weeks post engraftment, NRGL and HNFL mice of both sexes were inoculated via intra-fetal lung xenograft (intra-fLX) injection with $10^4$ or $10^6$ PFU of SARS-CoV-2 in 50 μL of sterile 1X PBS. Inoculations were performed under 1–3% isoflurane anesthesia. Either one or both implants were inoculated by direct injection into the fLX. Animals were euthanized at day two or day seven post inoculation.

### Tissue collection and lung inflation for histology

At the indicated endpoints, mice were anesthetized using 1–3% isoflurane, followed by euthanasia using an overdose of ketamine/xylazine.

### Virus

### SARS-CoV-2 isolate stock

All replication-competent SARS-CoV-2 experiments were performed in a BSL-3 facility at the Boston University National Emerging Infectious Diseases Laboratories. The clinical isolate named 2019-nCoV/USA-WA1/2020 strain (NCBI accession number: MN985325) of SARS-CoV-2 was obtained from BEI Resources (Manassas, VA, USA). To generate the passage 1 (P1) virus stock, Vero E6 cells, pre-seeded the day before at a density of 10 million cells, were infected in T175 flasks with the master stock, diluted in 10 mL final volume of Opti-MEM (ThermoFisher Scientific, Waltham, MA, USA). Following virus adsorption to the cells at 37°C for 1 h, 15 mL DMEM containing 10% FBS and 1X penicillin/streptomycin was added to the flask. The next day, media was removed, the cell monolayer was rinsed with 1X PBS, pH 7.5 (ThermoFisher Scientific) and 25 mL of fresh DMEM containing 2% FBS was added. Two days later, when the cytopathic effect of the virus was clearly visible, culture medium was collected, filtered through a 0.22 μm filter, and stored at −80°C. Our P2 working stock of the virus was prepared by infecting Vero E6 cells with the P1 stock, at a multiplicity of infection (MOI) of 0.1. Cell culture media was harvested at 2DPI and 3DPI, and after the last harvest, ultracentrifuged (Beckman Coulter Optima L-100k; SW32 Ti rotor) for 2 h at 25,000 rpm (80,000 x $g$) over a 20% sucrose cushion (Sigma-Aldrich). Following centrifugation, the media and sucrose were discarded, and pellets were left to dry for 5 min at room temperature. Pellets were then resuspended overnight at 4°C in 500 μL of 1X PBS. The next day, concentrated virions were aliquoted and stored at −80°C.

### Production of recombinant SARS-CoV-2 expressing NanoLuc luciferase

A recombinant SARS-CoV-2 expressing NanoLuc Luciferase (rSARS-CoV-2 NL) (Xie et al., 2020) was graciously provided by the Laboratory of Pei-Yong Shei. To propagate the virus, a day prior to propagation 10 million Vero E6 cells were seeded in a T-175 flask, 10 μL of rSARS-CoV-2 NL virus stock was diluted in 10 mL of OptiMEM. Virus was incubated on cells for 1 h at 37°C then 15 mL of DMEM containing 10% FBS and 1% penicillin/streptomycin was added. The next morning, media was removed, cells were washed with 1X PBS and 25 mL of fresh DMEM containing 2% FBS was added. Virus was incubated for an additional 48 h, supernatant was collected, filtered through a 0.22 μm filter, and stored at −80°C. Viral stock was thawed and concentrated by ultracentrifugation (Beckman Coulter Optima L-100k; SW32 Ti rotor) at 25,000 x $g$ for 2 h at 4°C on a 20% sucrose cushion (Sigma-Aldrich, St. Louis, MO). Media and sucrose were discarded, pellets were dried for 5 min at room temperature, then viral pellets were suspended in 100 μL of 1X PBS at 4°C overnight. On the next day, concentrated virus was aliquoted and stored at −80°C.

### SARS-CoV-2 titering

The titer of our viral stocks was determined by plaque assay. Vero E6 cells were seeded into a 12-well plate at a density of $2.5 \times 10^5$ cells per well and infected the next day with serial 10-fold dilutions of the virus stock for 1 h at 37°C. Following virus adsorption, each

well was supplemented with 1 mL of overlay media, consisting of 2X DMEM supplemented with 4% FBS and mixed at a 1:1 ratio with 2.4% Avicel (DuPont, Wilmington, DE, USA; RC-581). Three days later, the overlay media was removed, the cell monolayer was washed with 1X PBS and fixed for 1 h at room temperature with 10% neutral buffered formalin (ThermoFisher Scientific). Following formalin removal, fixed cells were then washed with 1X PBS and stained for 1 h at room temperature with 0.1% crystal violet (Sigma-Aldrich) prepared in 10% ethanol/water. After rinsing with tap water, the number of plaques was counted and the virus titer was calculated.

### Generation of AAV-Flt3LG

The pAB269 AAV backbone containing AAV2 ITRs was kindly provided by Markus Grompe (OHSU, Oregon, USA). The plasmid was digested with PacI/MluI HF. The FLT3 was PCR amplified from pAL119-FLT3L (Addgene, item #21910), and the TBG was amplified from pX602-AAV-TBG:NLS-SaCas9-NLS-HA-OLLAS-bGHpA; U6:BsaI-sgRNA (Addgene, item #61593). The FLT3, TBG, and BGH PCR products had 15 bp of overlapping sequence with adjacent inserts and backbone and were assembled with In-Fusion (Takara Bio, Mountain View, CA, USA) to create the final construct. AAV-293 cells (Agilent) at 50% confluency in 15 cm dishes were transfected via the calcium phosphate method with 22.5 $\mu$g XR8 (NGVB, Indianapolis, IN), 7.5 $\mu$g pHelper (Agilent), 7.5 $\mu$g of pAB269-TBG-FLT3 LG-BGH per plate. Media was collected every 24 h for 72 h total. After 72 h, the media was treated with a 5X solution of 40% PEG8000 and 2.5 M NaCl to precipitate the AAV for 2 h at 4°C before being spun down at 4300 x $g$ for 20 min. Cells from plates were scraped, washed with PBS, and resuspended in hypotonic buffer (10 mM HEPES, 1.5 mM MgCl2, 10 mM KCl, 0.35 mg/mL spermine) on ice for 10 min before 1 mL restore buffer (62.5% sucrose wt/vol in hypotonic buffer) was added. Cell membranes were sheared in a 15 mL Kontes Dounce homogenizer and nuclei were spun down at 500 x $g$ for 10 min. AAV from PEG precipitate was resuspended in 6 mL high salt buffer (2.5 mM KCl, 1 mM MgCl2, 1 M NaCl in PBS) and added to nuclei that had been resuspended in 1 mL low salt buffer (2.5 mM KCl, 1 mM MgCl2, in PBS). Lysate was treated with 250 units of Benzonase (Sigma) at 37°C for 30 min and then spun at 4300 x $g$ for 30 min before being loaded onto an iodixanol gradient. AAV was spun at 38,000 rpm in an SW41 rotor for 3 h at 16°C. AAV was collected from the 40% iodixanol layer and buffer was exchanged to AAV storage buffer (PBS with 35 mM NaCl, 0.002% pluronic F-68, 5% glycerol) in a 100 MWCO centrifugal filter column (MilliporeSigma, Burlington, MA, USA). Samples were analyzed via silver stain to check purity and qPCR to quantify.

### Tissue processing

#### Single cell suspension from whole blood

Blood (200 $\mu$L) was collected through submandibular bleeding and transferred into EDTA capillary collection tubes (Microvette 600 K3E; Sarstedt, Nümbrecht, Germany). Cells were separated from serum through centrifugation, and red blood cells were lysed with 1X lysis buffer (BD Pharm Lyse, BD Biosciences) for 15 min at room temperature in the dark. Following lysis and quenching with 10% (v/v) FBS DMEM media, blood cells were then washed twice with a 1% (v/v) FBS-PBS solution (FACS Buffer) before antibody staining.

#### Single cell suspension from fLX

Fetal lung xenografts were collected and placed in Roswell Park Memorial Institute Medium (RPMI) with 10% FBS. To generate single cell suspensions, lung tissues were placed on a 60 mm dish and minced using a disposable scalpel. Tissue pieces were transferred to a 15 mL conical tube with 3 mL of digestion buffer (HBSS minus $Ca^{2+}$, $Mg^{2+}$, and phenol red, 0.5 mg/mL Liberase TM, 1 mg/mL DNase I) and incubated at 37°C for 30 min with agitation every 10 min. Minced pieces were transferred to a 70 $\mu$m strainer on a 50 mL tube and mashed through using the plunger of a 3 mL syringe plunger. The strainer was washed two times with 1 mL of FACS buffer (1X PBS with 1% (v/v) FBS) and the cell suspension was centrifuged at 300 x $g$ for 5 min at 4°C. The cell pellet was resuspended in 1 mL of ACK lysing buffer (ThermoFisher Scientific; #A1049201) and incubated for 2 min at room temperature. After incubation, 9 mL of FACS buffer was added to quench the lysis, samples were centrifuged at 300 x $g$ for 5 min at 4°C, and the cell pellet was resuspended in 1 mL of FACS buffer prior to antibody staining.

#### Single cell suspension from spleen

Spleen was collected and placed in RPMI with 10% FBS. To generate single cell suspensions, a 70 $\mu$m strainer was placed into one well of a 6-well plate with 4 mL of FACS buffer. Whole spleen was then placed onto the strainer and mashed through the strainer using a 3 mL syringe plunger. After the strainer was washed twice with 1 mL of FACS buffer, the resultant single cell suspension was transferred to a 15 mL conical tube and samples were centrifuged at 300 x $g$ for 5 min at 4°C. The cell pellet was resuspended in 1 mL of ACK lysing buffer and incubated for 2 min at room temperature. After incubation, 9 mL of FACS buffer was added to quench the lysis, samples were centrifuged at 300 x $g$ for 5 min at 4°C, and the cell pellet was resuspended in 1 mL of FACS buffer.

### RNA extraction

#### Generation of cell lysates for total RNA extractions

Tissues were collected from mice and placed in 600 $\mu$L of RNAlater (MilliporeSigma: #R0901500ML) and stored at −80°C. For processing, 20–30 mg of tissue was taken and placed into a 2 mL tube with 600 $\mu$L of RLT buffer with 1% $\beta$–mercaptoethanol and a 5 mm stainless steel bead (Qiagen, Hilden, Germany: #69989). Tissues were then dissociated using a Qiagen TissueLyser II (Qiagen) with the following cycle: two min dissociation at 1800 oscillations/min, one min rest, two min dissociation at 180 oscillations/min. Samples were then subject to centrifugation at 13,000 rpm for 10 min at room temperature and supernatant was transferred to a new 1.5 mL tube. RNA extractions were performed using a Qiagen RNeasy Plus Mini Kit (Qiagen: #74134), according to the manufacturer's

instructions, with an additional on-column DNase treatment (Qiagen: #79256). RNA was eluted in 30 µL of RNase/DNase free water.

*RNA extraction from serum*

Viral RNA was extracted from serum using a Zymo Viral RNA extraction kit (Zymo Research, Irvine, CA, USA: #R1035) following the manufacturers protocol. Briefly, serum was mixed with RNA/DNA shield (Zymo) at a 1:1 ratio. RNA buffer was then added to the serum (2:1 ratio) and passed through a column by centrifugation at 13,000 x *g*. The column was then washed twice, and RNA was eluted with 15 µL of RNase/DNase free water.

### Flow cytometry

For all flow cytometry experiments, flowcytometric analysis was performed using an LSRII Flow Cytometer (BD Biosciences). Flow cytometry fluorophore compensation for antibodies was performed using an AbC[TM] Anti-Mouse Bead Kit (ThermoFisher Scientific). Flow cytometry data were analyzed using FlowJo software (TreeStar, Ashland, OR, USA).

*Antibodies*

From BioLegend (San Diego, CA, USA): CD45-PE-Cy7 clone 30-F11, CD45-PE-Dazzle5 clone 30-F11. The following anti-human antibodies were used for flow cytometry: from BD Biosciences (San Jose, CA, USA): CD45-V500 clone H130, CD34-FITC clone 581, CD8-FITC clone G42-8, CD11c-allophycocyanin clone B-ly6; from BioLegend: CD56-allophycocyanin-Cy7 clone HCD56, HLA-DR-BV510 clone L243, CD3-BV605 clone UCHT1, CD20-BV650 clone 2H7, CD16-BV117 clone B73.1, CD45-BV785 clone H130, CD8-FITC clone RPA-T8, CD33-PE clone WM53, CD14-PerCP-Cy5.5 clone HCD14, CD45RA-PE-Cy7 clone HI100, CD56-allophyco-cyanin clone QA17A16, CD4-Alexa Fluor 700 clone SK3; from Thermo Scientific: CD14-Alexa 700 clone Tuk4, CD3-PE-Cy5.5 clone 7D6, CD4-PE clone RPA-T4, CD19-PacBlue clone SJ25C1, CD16-PE-TexasRed clone 3G8.

*Quantification of peripheral human chimerism in HNFL mice*

$2-4 \times 10^6$ PBMCs of human or murine origin were isolated as described above and stained for 1 h at 4°C in the dark with an antibody cocktail targeting human(h)CD45, mouse CD45, hCD3, hCD4, hCD8, hCD16, hCD19, hCD11c, hCD56 and hCD14. Following washing with FACS Buffer, cells were fixed with fixation buffer (1% (v/v) FBS, 4% (w/v) PFA in PBS) for 30 min at 4°C in the dark. Chimerism of all humanized mice was assessed by quantifying the following human populations: Human CD45^{+}, human CD45^{+} murine CD45^{-}; T-cells, CD45^{+} CD3^{+}; CD4^{+} T cells, CD45^{+} CD3^{+} CD4^{+}; CD8^{+} T cells, CD45^{+} CD3^{+} CD8^{+}; CD45^{+} CD16^{+} leukocytes; B-cells, CD45^{+} CD19^{+}; conventional dendritic cells, CD45^{+} CD11c^{+}; NK/NKT cells, CD45^{+} CD56^{+}; Monocytes, CD45^{+} CD14^{+}.

*Antibody staining and flow cytometry analysis of HNFL fLX*

After generation of single cell suspension, $5 \times 10^5$ - $1 \times 10^6$ cells were used for flow cytometry staining. Cells were centrifuged at 300 X *g* for 5 min at 4°C. The cell pellet was resuspended in a mix of 22.5 µL FACS buffer and 2.5 µL of FcX (Biolegend; #422302) and incubated for 10 min at room temperature. After blocking, 25 µL of antibody cocktail targeting hCD3, hCD20, hCD16, hHLA-DR, hCD45, hCD8, hCD4, hCD33, hCD45RA, hCD56, hCD14, mCD45, and containing a LIVE/DEAD viability dye (ThermoFisher Scientific) was added to each sample and incubated in the dark for 30 min at 4°C. After staining, 1 mL of FACS buffer was added to each sample, samples were centrifuged at 300 x *g* for 5 min, washed with 1 mL FACS buffer, centrifuged at 300 x *g* for 5 min, and then fixed in 200 µL 4% PFA for 30 min. After fixation cells were washed twice with 1 mL FACS buffer, resuspended in FACS buffer, and stored protected from light at 4°C until analysis. Human immune cell subsets were gated as follows: human CD45^{+}, hCD45^{+} mCD45^{-}; human CD3^{+}, hCD45^{+} hCD3^{+}; human CD4^{+}, hCD45^{+} hCD3^{+} hCD4^{+}; human CD8^{+}, hCD45^{+} hCD3^{+} hCD8^{+}; CD20^{+}, hCD45^{+} hCD3^{-} hCD20^{+}; human CD56^{+}, hCD45^{+} hCD3^{-} hCD20^{-} hCD33^{-} hCD56+.[+].

### Viral quantification

*SARS-CoV-2 RT-qPCR*

To determine SARS-CoV-2 RNA copies, RT-qPCR for SARS-CoV-2 E protein was performed using a One-Step Taqman-based system. Briefly, a 20 µL reaction mixture containing 10 µL of Quanta qScript[TM] XLT One-Step RT-qPCR ToughMix® (VWR, Radnor, PA, USA; #76047–082), 0.5 µM Primer E_Sarbeco_F1 (ACAGGTACGTTAATAGTTAATAGCGT), 0.5 µM Primer E_Sarbeco_R2 (ATATTGCAGCAGTACGCACACA), 0.25 µM Probe E_Sarbeco_P1 (FAM-ACACTAGCCATCCTTACTGCGCTTCG-BHQ1), and 2 µL of total RNA was subjected to One-Step RT-qPCR using Applied Biosystems QuantStudio 3 (ThermoFisher Scientific), with the following cycling conditions; reverse transcription for 10 min at 55°C and denaturation at 94°C for 3 min followed by 45 cycles of denaturation at 94°C for 15 s and annealing/extension at 58°C for 30 s. Ct values were determined using QuantStudio[TM] Design and Analysis software V1.5.1. Calculations for RNA copies/mL were determined using a SARS-CoV-2 E RNA as a standard.

*Quantification of infectious particles by plaque assay*

SARS-CoV-2 infectious particles in inoculated fLX were quantified by plaque assay. After euthanizing mice, tissues were collected in 500 µL of RNAlater (MilliporeSigma: #R0901500ML) and stored at −80°C. The day prior to experiments, $8 \times 10^4$ cells per well were seeded in a 24-well plate. Between 20 and 30 mg of tissue was placed into 500 µL of OptiMEM (ThermoFisher Scientific). Tissues were homogenized using a Qiagen TissueLyser II (Qiagen) by two dissociation cycles (two min at 1800 oscillations/min) with one min rest in between. Samples were then subjected to centrifugation at 13,000 rpm for 10 min at room temperature, and supernatant was transferred to a new 1.5 mL tube. From this, $1:10^2–1:10^7$ dilutions were made in OptiMEM and 200 µL of each dilution were plated onto a 24-well plate. Supernatant was incubated at 37°C for 1 h with gentle rocking of the plate every 10 min. After viral adsorption, 1 mL a 1:1 mixture of 2X DMEM 4% FBS and 2.4% Avicel (Dupont) was overlaid into each well. Plates were incubated for 72 h at 37°C with 5% $CO_2$. Avicel was then removed, cells were washed twice with 1X PBS, and then cells were fixed in 10% buffered formalin

(ThermoFisher Scientific) for 1 h. After fixation, formalin was removed, and cells were stained with 0.1% crystalline violet in 10% ethanol/water for 1 h and washed with tap water. Number of plaques were counted, and infectious particles (PFU/mg of tissue) were calculated.

### Histology and microscopy
#### Histologic processing and analysis
Tissue samples were fixed for 72 h in 10% neutral buffered formalin, processed in a Tissue-Tek VIP-5 automated vacuum infiltration processor (Sakura Finetek USA, Torrance, CA, USA), followed by paraffin embedding using a HistoCore Arcadia paraffin embedding station (Leica, Wetzlar, Germany). Generated formalin-fixed, paraffin-embedded (FFPE) blocks were sectioned to 5 μm using an RM2255 rotary microtome (Leica), transferred to positively charged slides, deparaffinized in xylene, and dehydrated in graded ethanol. Tissue sections were stained with hematoxylin and eosin for histologic examination, while unstained slides were used for immunohistochemistry. Qualitative and semi-quantitative histomorphological analyses were performed by a single board-certified veterinary pathologist (N.A.C.). An ordinal scoring system was developed to capture the heterogeneity of histologic findings in fLX. Individual histologic findings that were scored included: syncytial cells, hyaline membrane, intra-airspace neutrophils and necrosis, hemorrhage, edema, denuded pneumocytes, capillary fibrin thrombi, intermediate vessel fibrin thrombi and coagulative necrosis. The entire fLX was examined at 200x with a DM2500 light microscope (Leica) using the following criteria: 0 = not present, 1 = found in <5% of fields, 2 = found in >5% but <25% of fields, or 3 = found in >25% of fields. Several criteria were also restricted to 'not observed' (0) or 'observed' (1). Scores were combined to generate a cumulative lung injury score.

#### Antibodies
The following primary antibodies were used: anti-human CD31 clone JC/70A (Biocare Medical, Pacheco, CA, USA), anti-mouse CD31 clone D8V9E (Cell Signaling Technology, Danvers, MA, USA), ACE2 clone EPR34435 (Abcam, Waltham, MA, USA), polyclonal SFTPC (Seven Hills Bioreagents, Cincinnati, OH, USA), anti-human CD68 clone KP1 (LS Bio, Seattle, WA, USA), anti-human CD61 clone ARC0460 (Thermo Scientific), polyclonal anti-human CD3 (Dako) and anti-human CD8 clone SP57 (Roche, Basel, Switzerland), and anti-human CD20 clone L26 Dako Omnis (Agilent, Santa Clara, CA, USA). The secondary antibody used in this study included HRP Goat anti-Rabbit IgG (H&L) (Vector Laboratories, Burligame, CA, USA). For mouse derived primary antibodies, a linker antibody (Abcam) was used prior to application of the secondary antibody to prevent non-specific binding. DAB and purple chromogens (Roche) and chromogens used for TSA-conjugated Opal 480, 520, 570, 620, and 690 fluorophores (Akoya Biosciences, Marlborough, MA, USA) were utilized to develop immunohistochemical assays. The following anti-SARS-CoV-2 antibodies were used for immunohistochemistry: rabbit polyclonal anti-SARS-CoV Nucleoprotein (Novus Biological, Littleton, CO, USA), mouse monoclonal anti-SARS-CoV-2 Spike clone 2B3E5 (This antibody was used in this study as clone E7U60, which was the pre-production clone ID of clone 2B3E5; Cell Signaling Technology).

#### Multispectral fluorescent imaging
Fluorescently labeled slides were imaged using either a Mantra 2.0™or Vectra Polaris™ Quantitative Pathology Imaging System (Akoya Biosciences). To maximize signal-to-noise ratios, fluorescently acquired images were spectrally unmixed using a synthetic library specific for the Opal fluorophores used in each assay plus DAPI. An unstained fLX section was used to create an autofluorescence signature that was subsequently removed from multispectral images using InForm software version 2.4.8 (Akoya Biosciences).

#### Image analysis of multiplex immunohistochemistry
Digitized whole slide scans were analyzed using the image analysis software HALO v3.2 (Indica Labs, Inc., Corrales, NM, USA). Slides were manually annotated to select regions of interest, excluding accessory skin and adipose tissue, to ensure inclusion of only the fLX. Visualization thresholds were adjusted in viewer settings to minimize background signal identification and maximize specificity of signals for each sample. Quantitative positive pixel analysis outputs were obtained using the Area Quantification (AQ) module, which reports total area of immunoreactivity of a specified parameter within a region of annotated interest. Values are given as a percentage of total tissue area analyzed. Minimum dye intensity thresholds were established using the real-time tuning field of view module to accurately detect positive immunoreactivity. For quantitative cellular phenotyping, the fluorescence Highplex (HP) module was utilized. Cells are identified using DAPI to segment individual nuclei. Minimum cytoplasm and membrane thresholds are set for each dye to detect positive staining within a cell. Parameters are set using the real-time tuning mechanism that was tailored for each individual biopsy based on signal intensity. Phenotypes are determined by selecting inclusion and exclusion parameters relating to stains of interest. This algorithm produces a quantitative output for each cell phenotype standardized to the area analyzed (cells/μm2).

#### Transmission electron microscopy
Tissue samples were fixed for 72 h in a mixture of 2.5% glutaraldehyde and 2% formaldehyde in 0.1 M sodium cacodylate buffer (pH 7.4). Samples were then washed in 0.1 M cacodylate buffer and postfixed with 1% osmiumtetroxide (OsO4)/1.5% potassiumferrocyanide (KFeCN6) for 1 h at room temperature. After washes in water and 50 mM maleate buffer pH 5.15 (MB), the samples were incubated in 1% uranyl acetate in MB for 1 h, washed in MB and water, and dehydrated in grades of alcohol (10 min each: 50%, 70%, 90%, 2 × 10 min 100%). The tissue samples were then put in propyleneoxide for 1 h and infiltrated overnight in a 1:1 mixture of propyleneoxide and TAAB Epon. The following day the samples were embedded in fresh TAAB Epon and polymerized at 60°C for 48 h. Semi-thin (0.5 μm) and ultrathin sections (50–80 nm) were cut on a Reichert Ultracut-S microtome (Leica). Semi-thin sections were picked up on glass slides and stained with toluidine blue for examination by light microscopy to find affected areas in the tissue.

Ultrathin sections from those areas were picked up onto formvar/carbon coated copper grids, stained with 0.2% lead citrate and examined in a JEOL 1200EX transmission electron microscope (JOEL, Akishima, Tokyo, Japan). Images were recorded with an AMT 2k CCD camera.

### Proteomics and transcriptomic analysis
#### Mass spectrometry sample preparation

Protein extracts were generated by suspending tissue in a proteomic lysis buffer consisting of 100 mM Tris pH 8.5, 6M GuHCl, 1 mM CaCl2, 10 mM TCEP, and 40 mM Chloroacetamide. Tissues samples were homogenized using a Qiagen TissueLyser II (Qiagen; two min dissociation at 1800 oscillations/min, one min rest, two min dissociation at 180 oscillations/min) prior being inactivated at 95°C for 10 min. Inactivated protein extracts were sonicated with a Branson probe sonicator and were then quantified via Bradford assay. The samples were diluted with 100 mM Tris, pH 8.5 buffer to lower the GuHCl concentration to 0.75 M. Lysate proteins were then digested by adding trypsin (Pierce, Waltham, MA, USA) at a 1:50 ratio (enzyme:protein, w/w) and incubating the samples overnight at 37°C with shaking. Trypsin digestion was terminated with the addition of TFA to below pH 3 and the peptide digests were desalted via reversed-phase C18 columns (Sep-Pak, Waters, Mildford, MA, USA) with a wash buffer of 0.1% TFA and elution buffer of 60% acetonitrile. The desalted peptides were then quantified with a Quantitative Colorimetric Peptide Assay (Pierce). Each sample, comprising 100 μg peptides, was TMT-labeled with TMTPro 16plex reagents (ThermoFisher Scientific: # A44520) as per the manufacturer's protocol. Labeled peptides were again desalted on a C18 column prior to basic reversed-phase fractionation.

TMT-labeled peptides were fractionated via basic reversed-phase chromatography on the Agilent 1200 series HPLC instrument equipped with the XBridge Peptide BEH C18 column (130A°, 3.5 mm, 4.6 mm × 250 mm, Waters Corporation). Prior to loading peptides, the C18 column was washed with 100% methanol and equilibrated with Buffer A (0.1% ammonium hydroxide and 2% acetonitrile). Peptides were injected via the autosampler and eluted from the column using a gradient of mobile phase A (2% ACN, 0.1% NH4OH) to mobile phase B (98% ACN, 0.1% NH4OH) over 48 min at a flowrate of 0.4 mL/min. The 48 fractions collected were orthogonally concatenated into 12 pooled fractions. Three percent of each fraction was aliquoted and saved for global proteomic profiling and the remaining 97% of peptides were used for phosphopeptide enrichment using Fe-NTA magnetic beads (CubeBiotech, Monheim am Rhein, Germany) (Leutert et al., 2019). Briefly, the fractionated peptides were dried and resuspended in binding buffer (80% Acetonitrile and 01% TFA). Before being added to the peptides, the Fe-NTA beads were washed with binding buffer. Peptides were then incubated with the Fe-NTA bead slurry for 20 min in a Kingfisher Apex magnetic bead transferring system (ThermoFisher Scientific) before being moved into wash wells. Beads with bound phosphopeptides were washed twice in binding buffer, after which phosphopeptides were serially eluted twice by moving the beads into wells containing 200 μL of elution buffer (50% acetonitrile and 2.5% ammonium hydroxide). Both phosphopeptide eluates corresponding to an orthogonal fraction were combined prior to drying in a speedvac.

#### Mass spectrometry analysis

Multiplexed peptide fractions from each time point were resuspended in mobile phase A solvent (2% acetonitrile and 0.1% formic acid) to be analyzed on the Exploris 480 mass spectrometer equipped with FAIMS (ThermoFisher Scientific). The mass spectrometer was interfaced to the Easy nanoLC1200 HPLC system (ThermoFisher Scientific). Briefly, the peptides were first loaded onto a reverse-phase nanotrap column in mobile phase A, (75 mm i.d. 3 2 cm, Acclaim PepMap100 C18 3 mm, 100 A°, ThermoFisher Scientific) and separated over an EASY-Spray column, (ES803A, ThermoFisher Scientific) using a gradient (6%–19% over 58 min, then 19%–36% over 34 min) of mobile phase B (0.1% formic acid, 80% acetonitrile) at a flowrate of 250 nL/min. The mass spectrometer was operated in positive ion mode with a capillary temperature of 275°C and a spray voltage of 2500 V. All data was acquired with the mass spectrometer operating in data dependent acquisition (DDA) mode, with FAIMS cycling through one of three compensation voltages (−50V, −57V, −64V) at each full scan. Precursor scans were acquired at a resolution of 120,000 FWHM with a maximum injection time of 120 ms in the Orbitrap analyzer. The following 0.8 s were dedicated to fragmenting the most abundant ions at the same FAIMS compensation voltage, with charge states between 2 and 5, via HCD (NCE 33%) before analysis at a resolution of 45,000 FWHM with a maximum injection time of 60 ms. Phosphopeptides were analyzed in the same manner, save for the injection time being raised to 150 ms to allow for lower abundant analyte to fill the trap.

#### Analysis of raw mass spectrometry data

All acquired MS/MS spectra were simultaneously searched against the complete SwissProt human proteome (downloaded on 2020-10-20), the complete SwissProt mouse proteome (downloaded on 2020-10-20), and the Uniprot SARS-CoV-2 proteome (For side-by-side NRGL vs. HNFL experiment only; downloaded on 2020-05-03) using MaxQuant (Version 1.6.7.0), which integrates the Andromeda search engine. TMT reporter ion quantification was performed using MaxQuant with default settings. Briefly, enzyme specificity was set to trypsin and up to two missed cleavages were allowed. Cysteine carbamidomethylation was specified as fixed modification whereas oxidation of methionine and N-terminal protein acetylation were set as variable modifications. For phosphopeptides serine, threonine and tyrosine, phosphorylation were specified as variable modifications. Precursor ions were searched with a maximum mass deviation of 4.5 ppm and fragment ions with a maximum mass deviation of 20 ppm. Peptide and protein identifications were filtered at 1% FDR using the target-decoy database search strategy (Elias and Gygi, 2007). Proteins that could not be differentiated based on MS/MS spectra alone were grouped to protein groups (default MaxQuant settings). A threshold Andromeda score of 40 and a threshold delta score of 8 was applied to phosphopeptides. The MaxQuant output files designated ''Phospho(STY) sites'' and ''proteinGroups'' were filtered to remove entries that were either entirely mouse, or in the case of completely homologous

peptides, had annotations of both mouse and human. These two files, filtered to contain only accessions related to human proteins, were used for data normalization and other statistical analysis using in-house generated scripts in the R environment.

### Relative quantification of human ACE2 expression by RT-qPCR

RT-qPCR was performed using a Luna universal one-step RT-qPCR kit (number E3005L; New England Biolabs) on RNA extracted from naive NRGL-LX and HNFL-LX. RT-qPCR protocol was performed using the manufacturer's protocol with minor modifications. Briefly, 12 μL of reaction mixture containing 2 μL of RNA, 2 uL of each forward and reverse primer (10 uM), 0.6 μL of the 20X Luna WarmStart RT enzyme mix, and 6 μL of the 2X Luna universal one-step reaction mix was subjected to one-step RT-qPCR protocol using Applied Biosystems QuantStudio 3 (ThermoFisher Scientific), with the following cycling conditions: reverse transcription at 50°C for 10 min, initial denaturation at 95°C for 2 min followed by 40 cycles of denaturation at 95°C for 15 s and annealing/extension at 60°C for 1 min, ending with melt curve analysis from 65°C to 95°C, rising in 0.5°C/s increments, waiting for 30 s at 65°C and for 5 s at each step thereafter, and acquiring fluorescence at each temperature increment. The threshold cycle ($C_q$) values were determined using the QuantStudio Design and Analysis software V1.5.1. Human RPS11 was used as a reference gene and the human ACE2 $C_q$ values were normalized to human RPS11.

### Bulk RNA sequencing

Total RNA was processed from fLX as described above, and sent to BGI genomics (Hong Kong, China) for library preparation and sequencing (Pair-ends, 100 bp, 20M reads per sample). Raw FASTQ files were quality-checked with FastQC v0.11.7. Reads were found to be excellent quality and were aligned to the combined human (GRCh38, Ensembl 101) and mouse (GRCm38, Ensembl 101) genomes with STAR v2.7.1a followed by quantification with featureCounts v1.6.2. Quality was checked with MultiQC v1.6. All samples passed quality thresholds of >75% sequences aligned and >15 million aligned reads per sample. Significantly up- and downregulated genes were identified with DESeq2 v1.23.10 in R v3.6.0. Three treatment groups were compared to non-inoculated samples in turn: 2DPI, 7DPI and 7DPI contralateral. p-values were FDR-adjusted, and $\log_2$ fold change was shrunk with the *apeglm* method. Significance was determined by an FDR-adjusted $p < 0.01$ and a shrunken $\log_2$ fold change >2 or < −2. DESeq2 result were imported into Ingenuity Pathway Analysis (IPA; Service curated by Qiagen; Access provided through the Boston University Genome Science Institute) (Kramer et al., 2014), and a canonical pathway enrichment analysis was performed using the default settings and the same differential expression thresholds as before (shrunken log2 fold change >2 or < −2 and FDR-adjusted p value < 0.01).

### Single cell barcoding and sequencing

Following fLX processing into single cell suspension as described above, cells were frozen down in a 90% FBS (Bio-Techne, R&D systems) 10% DMSO solution (ThermoFisher Scientific) and kept at −80°C. Four to five days following freezing, cells were thawed, and viability was assessed using Trypan blue (Fisher Scientific). Samples with ≥90% viability were then processed using the Chromium Next GEM Single Cell 3′ GEM, Library & Gel Bead Kit v3.1, as per manufacturer instructions, and single cell barcoding was performed using a Chromium instrument (10x genomics) located in the NEIDL BSL-3. Reverse transcription of RNAs was performed in the BSL-3 using a thermocycler (Applied Biosciences), and cDNA was then removed from containment. Full-length, barcoded cDNAs were then amplified by PCR to generate sufficient mass for library construction. Enzyme fragmentation, A tailing, adaptor ligation and PCR were then performed at the Boston University single-cell sequencing core to obtain final libraries containing P5 and P7 primers used in Illumina bridge amplification. Size distribution and molarity of resulting cDNA libraries were assessed via Bioanalyzer High Sensitivity DNA Assay (Agilent Technologies, USA). All cDNA libraries were sequenced on an Illumina NextSeq 500 instrument at the Boston University microarray and sequencing core according to Illumina and 10x Genomics guidelines with 1.4–1.8 pM input and 1% PhiX control library spike-in (Illumina, USA).

### Preprocessing and quality control of single-cell data

The 10X CellRanger tool was used for demultiplexing, alignment, identification of cells, and counting of unique molecular indices (UMIs). Specifically, the CellRanger *makefastq* command was used to demultiplex raw base call (BCL) files generated by Illumina sequencers into FASTQ files. The CellRanger *count* command was used to perform alignment and create UMI count matrices using parameters –expect-cells = 6000. Multiple sequence alignments were performed. The reads were first aligned to the combined GRCh38 & mm10 reference. DecontX (Yang et al., 2020b) was then applied to estimate the cell contamination scores. The reads were then aligned to the GRCh38 and mm10 references individually, separating the mouse and human cells. Cells with more than 350 human counts and less than 250 mouse counts were classified as human, and vice versa. Finally, the reads were also aligned to a custom reference constructed by adding the SARS-CoV-2 transcriptome to the GRCh38 reference genome. Droplets with at least 500 UMIs underwent further quality control with the SCTK-QC pipeline [REF]. The median number of UMIs was 2,685, the median number of genes detected was 934, the median percentage of mitochondrial reads was 0%, and the median contamination estimated by decontX (Yang et al., 2020b) was 2% across cells from all samples. Cells with less than 3 counts, less than 3 genes detected were excluded leaving a total of 42,182 cells for the downstream analysis.

### Clustering of single-cell data with celda

The *celda* package was used to biclustering genes into modules and cells into subpopulations (Wang et al., 2020). The 5,000 most variable features were selected using the *seuratFindHVG* function from the *singleCellTK* package after excluding features with less than 3 counts in 3 cells. The *recursiveSplitModule* and *recursiveSplitCell* functions were used to select the model with 150 modules and 15 cell subpopulations after examining the Rate of Perplexity Change (RPC). Cells were embedded in two dimensions with UMAP using the *celdaUmap* function. Heatmaps for specific modules were generated using the *moduleHeatmap* function. Markers for each

cluster were identified with the *findMarkerDiffExp* function from the *singleCellTK* package using the parameters MAST algorithm (Finak et al., 2015) and parameters FDR threshold = 0.05. Clusters were annotated manually based on the level of expression of cluster defining genes and can be found in Table S1.

*Single-cell RNA sequencing datasets from human lung autopsy samples of patients with severe COVID19*

We took advantage of previously reported scRNAseq analysis (Delorey et al., 2021) on an autopsy cohort of 17 donors (eleven male and six females) with severe COVID19. Scaled mean expression of each PDG in lung monocyte/macrophage clusters were extracted and analyzed using the Broad Institute Single cell Portal (https://singlecell.broadinstitute.org/single_cell/study/SCP1052/covid-19-lung-autopsy-samples).

*In vivo* **imaging and data analysis**

NRGL mice were infected with $10^6$ PFU of rSARS-CoV-2 NL virus via direct fLX inoculation. For imaging, mice were injected with 5 μg (0.25 mg/kg) furimazine substrate (MedChemExpress, Monmouth Junction, NJ, USA) via tail-vein intravenous injection. Mice were then imaged using a 3D-imaging mirror gantry isolation chamber (InVivo Analytics, New York, NY, USA) and an IVIS Spectrum imager (PerkinElmer, Waltham, MA, USA). Briefly, mice were anesthetized using isoflurane (2.5%), placed into a body conforming animal mold (BCAM) (InVivo Analytics) and imaged within 5 min of injection. Mice were imaged using a sequence imaging file as follows: 60 s open filter, 240 s 600 nM, 60 s open, 240 s 620 nm, 60 s open, 240 s 640 nm, 60 s open, 240 s 660 nm, 60 s open, 240 s 680 nm, 60 s open using an IVIS Spectrum imager (PerkinElmer). Data analysis of planar imaging was conducted using LivingImage (PerkinElmer). 3D reconstitution of bioluminescence signals was conducted manually by InVivo Analytics.

## QUANTIFICATION AND STATISTICAL ANALYSIS

For histopathological score, viral loads/titers comparison and Spike quantification, Kruskal-Wallis, Kolmogorov-Smirnov non-parametric t test, or a two-way ANOVA with Benjamini, Krieger, and Yekutieli correction for multiple comparisons were applied given the non-continuous nature of the data (i.e., viral inoculation in areas displaying differential stage of tissue development, and/or differences in fLX engraftment, and/or donor/gestational age differences). A two-way ANOVA with Benjamini, Krieger, and Yekutieli correction for multiple comparisons was also used to generate the ISG p.value heatmap given the non-parametric nature of these data. Significance between HNFL-LX viral RNA copies values and area of productive infection was calculated by running a Kruskal-Wallis test between pooled viral RNA copies/mg tissue values from inoculated HNFL-LX (n = 7) and NRGL-LX (n = 14, all values above PIT). For quantitative analysis of hematopoietic cell infiltration (i.e. multiplex IHC and flow cytometry data), Welch's t test or one-way ANOVA tests were used. For comparison of viral gene count between macrophage clusters and other clusters, a Mann-Whitney t test was used. For comparison of combined PDG expression between clusters, an RM one-way ANOVA with Geisser Green-house correction was used. All statistical tests and graphical depictions of results were performed using GraphPad Prism version 9.0.1 software (GraphPad Software, La Jolla, CA). For all tests, $p \leq 0.05$ was considered statistically significant. Statistical significance on figures and supplemental figures is labeled as follow: $*p \leq 0.05$, $**p \leq 0.01$, $***p \leq 0.001$, $****p \leq 0.0001$.